Three-dimensional distribution of a major desert dust outbreak over East Asia in March 2008 derived from IASI satellite observations

Juan Cuesta, Maxim Eremenko, Cyrille Flamant, Gaëlle Dufour, Benoit Laurent, Gilles Bergametti, Michael Höpfner, Johannes Orphal, Daniel Zhou

AGU PUBLICATIONS

JGR

Journal of Geophysical Research: Atmospheres

RESEARCH ARTICLE
10.1002/2014JD022406

Key Points:
- First satellite observation of the 3D evolution of dust plumes over land and sea
- Good agreement between dust vertical distribution derived from IASI and CALIOP
- Analysis of downward mixing of dust layers in convective marine boundary layers

Correspondence to:
J. Cuesta,
cuesta@lisa.u-pec.fr

Citation:
Cuesta, J., M. Eremenko, C. Flamant, G. Dufour, B. Laurent, G. Bergametti, M. Höpfner, J. Orphal, and D. Zhou (2015), Three-dimensional distribution of a major desert dust outbreak over East Asia in March 2008 derived from IASI satellite observations, *J. Geophys. Res. Atmos.*, *120*, doi:10.1002/2014JD022406.

Received 6 AUG 2014
Accepted 17 JUN 2015
Accepted article online 18 JUN 2015

Three-dimensional distribution of a major desert dust outbreak over East Asia in March 2008 derived from IASI satellite observations

Juan Cuesta[1], Maxim Eremenko[1], Cyrille Flamant[2], Gaëlle Dufour[1], Benoît Laurent[1], Gilles Bergametti[1], Michael Höpfner[3], Johannes Orphal[3], and Daniel Zhou[4]

[1]Laboratoire Interuniversitaire des Systèmes Atmosphériques, UMR CNRS 7583, Université Paris Est Créteil, Université Paris Diderot, Créteil, France, [2]Sorbonne Universités, UPMC Université Paris 06, CNRS & UVSQ, UMR 8190, LATMOS, Paris, France, [3]Karlsruher Institut für Technologie, Institut für Meteorologie und Klimaforschung, Karlsruhe, Germany, [4]NASA Langley Research Center, Hampton, Virginia, USA

Abstract We describe the daily evolution of the three-dimensional (3D) structure of a major dust outbreak initiated by an extratropical cyclone over East Asia in early March 2008, using new aerosol retrievals derived from satellite observations of IASI (Infrared Atmospheric Sounding Interferometer). A novel auto-adaptive Tikhonov-Phillips-type approach called AEROIASI is used to retrieve vertical profiles of dust extinction coefficient at 10 μm for most cloud-free IASI pixels, both over land and ocean. The dust vertical distribution derived from AEROIASI is shown to agree remarkably well with along-track transects of CALIOP spaceborne lidar vertical profiles (mean biases less than 110 m, correlation of 0.95, and precision of 260 m for mean altitudes of the dust layers). AEROIASI allows the daily characterization of the 3D transport pathways across East Asia of two dust plumes originating from the Gobi and North Chinese deserts. From AEROIASI retrievals, we provide evidence that (i) both dust plumes are transported over the Beijing region and the Yellow Sea as elevated layers above a shallow boundary layer, (ii) as they progress eastward, the dust layers are lifted up by the ascending motions near the core of the extratropical cyclone, and (iii) when being transported over the warm waters of the Japan Sea, turbulent mixing in the deep marine boundary layer leads to high dust concentrations down to the surface. AEROIASI observations and model simulations also show that the progression of the dust plumes across East Asia is tightly related to the advancing cold front of the extratropical cyclone.

1. Introduction

Desert dust storms strongly affect the environment and significantly contribute to climate forcing [e.g., *Yoshioka et al.*, 2007; *Mahowald et al.*, 2001]. Numerous studies have shown major impacts of desert dust on the Earth radiative budget, atmospheric dynamics, and chemical and biogeochemical balances [e.g., *Haywood and Boucher*, 2000; *Jones et al.*, 2004; *Dunion and Velden,* 2004; *Su et al.*, 2010; *Mahowald et al.*, 2005]. Desert dust directly impacts economic activities and human health by imposing low visibility and poor air quality, respectively, in populated regions downwind from deserts [e.g., *Xu et al.*, 1994; *Prospero*, 1999; *Mahowald et al.*, 2007; *Wang et al.*, 2012]. This occurs for example in large megacities of northeastern Asia (e.g., Beijing) regularly affected by dust outbreaks originating from the Mongolian and Chinese deserts (e.g., Gobi and Taklimakan) in winter and spring [e.g., *Sun et al.*, 2001; *Laurent et al.*, 2006; *Zhang et al.*, 2012]. The degradation of air quality associated with dust storms may have severe sanitary consequences on the population of these megacities, as they are also prone to heavy anthropogenic pollution [e.g., *Molina and Molina*, 2004]. At the regional scale, the impact of desert dust will depend on the vertical distribution of dust plumes resulting from long-range transport. Dust layers can impact chemical balances, atmospheric stability, or cloud properties at all altitudes and depending on the altitude at which they are transported. Near the surface, dust can directly affect air quality and settle down on the surface by dry deposition. The quantification of such impacts are highly uncertain, particularly due to the sporadic character of dust emissions as well as the large variability of dust properties [e.g., *d'Almeida*, 1987; *Dubovik et al.*, 2002] and occurrence linked to the meteorological controls [e.g., *Laurent et al.*, 2006].

Satellite observations play a fundamental role in describing the horizontal distribution of dust plumes and their transport in the atmosphere. The first approaches designed to depict the location of dust plumes over bright arid deserts were based on semiquantitative indicators, retrieved in the UV using observations

from TOMS (Total Ozone Mapping Spectrometer) [*Prospero et al.*, 2002; *Chiapello et al.*, 2005], OMI (Ozone Monitoring Instrument), GOME (Global Ozone Monitoring Experiment), and GOME-2 [*Torres et al.*, 2007], and also in the thermal infrared (TIR) using observations from AVHRR (Advanced Very High Resolution Radiometer) [*Ackerman*, 1997] and SEVIRI (Spinning Enhanced Visible and Infrared Imager) [*Legrand et al.*, 2001; *Schepanski et al.,* 2007, 2012; *Brindley et al.,* 2012]. Quantitative estimates of the horizontal distribution of columnar dust amounts are typically done in terms of aerosol optical depth (AOD). AODs can be derived from MODIS (Moderate-Resolution Image Spectroradiometer) observations over nondesert scenes based on visible and near-infrared measurements using the Dark-Target method [*Remer et al.*, 2005] or over deserts and other land surfaces (e.g., vegetated land covers) in the blue spectral region using the DeepBlue approach [*Hsu et al.,* 2004; *Sayer et al.*, 2013]. Dust-related AODs are also typically retrieved in the spectral domains from the UV to the near infrared using observations from e.g. OMI [*Torres et al.*, 2007], SeaWIFS (Sea-Viewing Wide Field-of-View Sensor) [*Diner et al.,* 2001; *Hsu et al.,* 2004], POLDER (Polarization and Directionality of the Earth's Reflectances) [*Su et al.*, 2010], MISR (Multi-angle Imaging Spectroradiometer) [*Diner et al.,* 2001], and SEVIRI [*Carrer et al.*, 2010; *Banks et al.*, 2013]. Recently, AODs associated with the horizontal distribution of Saharan dust plumes have also been derived on a daily basis using TIR hyperspectral measurements from AIRS (Atmospheric Infrared Sounder) [*DeSouza-Machado et al.*, 2010] and IASI (Infrared Atmospheric Sounder Interferometer) [*Klüser et al.*, 2012; *Vandenbussche et al.*, 2013]. These Infrared observations have also been used to detect and retrieve optical and microphysical properties of different types of aerosols [*Clarisse et al.,* 2010, 2013] and also coarse dust effective size on a monthly basis [*Pierangelo et al.*, 2005; *Peyridieu et al.*, 2013; *Capelle et al.*, 2014].

The vertical distribution of aerosols in the atmosphere can be obtained at high spatial resolution thanks to the ranging capability of CALIOP (Cloud-Aerosol Lidar with Orthogonal Polarization), a nadir pointing spaceborne lidar flown onboard the CALIPSO (Cloud-Aerosol Lidar and Infrared Pathfinder Satellite Observations) satellite since 2006 [*Winker et al.,* 2007, 2009]. However, only aerosol plumes located within the narrow footprint of the lidar (90 m width) are sampled along the CALIPSO track which makes it difficult to monitor the displacement of a plume as CALIPSO tracks (either nighttime or daytime) are spaced by about 24 degrees of longitude on a given day at midlatitudes. Nevertheless, the three-dimensional (3D) distribution of aerosols may be derived from CALIOP at seasonal and inter-annual scales [e.g., *Yu et al.*, 2010]. On the other hand, TIR passive hyperspectral sounders have also shown promising skills for deriving the vertical distribution of desert dust. Monthly mean altitudes of dust layers have been retrieved from AIRS [*Pierangelo et al.,* 2004] and IASI [*Peyridieu et al.*, 2013; *Capelle et al.*, 2014] over the ocean. Daily observations of the vertical distribution of Saharan dust plumes have also been derived so far mostly over ocean and for a limited fraction of cloud-free pixels over land, both in terms of layer top heights from AIRS [*DeSouza-Machado et al.*, 2010] and vertical profiles of dust concentration from IASI [*Vandenbussche et al.*, 2013]. However, until now, there existed no satellite-based approach allowing for the observation of the continuous 3D distribution of dust plumes over all surfaces (both over land and ocean) with full cloud-free coverage and on a daily basis.

In this paper, we use new aerosol retrievals derived from IASI observations to describe the 3D evolution of a major dust outbreak occurring over East Asia during 3 days in early March 2008 (from 1 to 3 March). For this, we have developed a new method called AEROIASI designed to retrieve vertical profiles of dust extinction coefficient at 10 μm from most IASI cloud-free pixels, both over land and ocean. AEROIASI enables the description of the 3D distribution of dust plumes for each IASI overpass, thereby providing a frame for the analysis of their spatiotemporal evolution. The horizontal resolution of IASI measurements is moderately coarse, corresponding to circular 12 km diameter pixels with centers spaced by 25 km (at nadir) and global coverage twice a day [at approximately 0930 and 2130 LT (local time)]. The IASI instrument is in orbit onboard MetOp-A since 2006 and is expected to provide continuous observations until 2022 thanks to measurements from the MetOp-B platform launched in 2012 and to measurements scheduled on MetOp-C [*Clerbaux et al.,* 2009]. We describe the new AEROIASI method and the related sensitivity analyses in sections 2.1 and 2.2, respectively. We then compare AEROIASI-derived dust vertical distributions with CALIOP retrievals along CALIPSO transects over East Asia on 1–3 March 2008 (section 2.3) and standard AOD retrievals from AERONET (Aerosol Robotic Network) [*Holben et al.*, 1998] sun photometers (section 2.4). Additional data sets used in the paper are briefly described in section 3. Then, section 4 presents the case study of dust outbreak over East Asia and the complex structure of the dust plumes resulting from long-range transport toward the Sea, using AEROIASI and other complementary data sets [i.e., MODIS observations, model

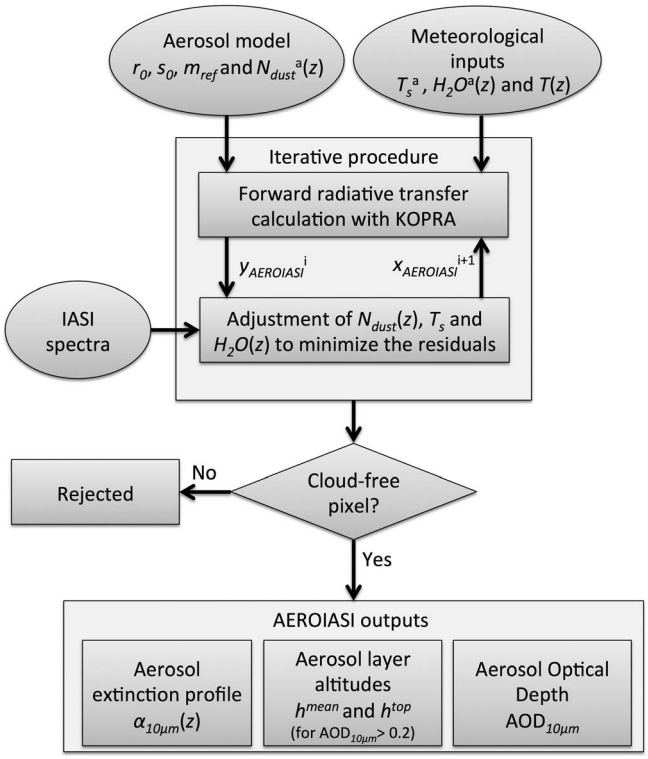

Figure 1. Flowchart of the AEROIASI approach.

simulations of dust from CHIMERE (e.g., *Menut et al.,* 2013), and meteorological reanalysis]. As discussed in section 4, AEROIASI retrievals allow to shade light with unprecedented details on processes responsible for the distribution of dust over northeast China and adjacent seas for this case study, namely atmospheric circulations associated with gap winds and fronts, as well as surface-atmosphere interactions and turbulence within the boundary layer. Conclusions are given in section 5.

2. Desert Dust Observations From AEROIASI

2.1. Methodology

The AEROIASI retrieval scheme has been conceived to derive vertical profiles of desert dust, in terms of extinction coefficient at 10 μm, from individual thermal infrared spectra measured by IASI. It is a constrained-least-squares fit method, based on explicit radiative transfer calculations, where the vertical distribution and abundance of dust are iteratively adjusted in order to fit IASI observations. This approach uses auto-adaptive constraints (see below) for adjusting simultaneously the dust profile and surface temperature in order to offer particularly good adaptability for different atmospheric and surface conditions. This unprecedented flexibility makes the aerosol retrieval possible for most cloud-free IASI pixels, both over ocean and land (even for bright surfaces and relatively low aerosol loads). The information on the vertical distribution of dust is mainly provided by their broadband radiative effect, which includes aerosol thermal emission depending at each altitude on the vertical profile of temperature (assuming local thermal equilibrium; see details in section 2.2).

The AEROIASI algorithm follows the sequence of steps presented in the flowchart of Figure 1. First, a desert dust model (including dust microphysical properties) and meteorological profiles are provided as inputs to the radiative transfer model. Then, a thermal infrared radiance spectrum is simulated and compared to the one measured by IASI, for selected spectral micro-windows. In order to minimize the spectral residuals, the method adjusts iteratively the radiative transfer inputs (e.g., the aerosol vertical profile) until reaching convergence (i.e., a relative minimum of the spectral residuals within the iterative procedure). Next, a series of cloud screening tests are performed. Then, the final outputs of AEROIASI are calculated for individual unscreened pixels. Each of these steps is detailed in the following paragraphs.

The climatological desert dust model used as input for the radiative transfer calculations consists of refractive indices and a single-mode lognormal particle size distribution (see details in Table 1). Refractive indices are taken from the mineral dust models of the GADS/OPAC database [*Hess et al.*, 1998] derived from Saharan dust (note that Saharan dust refractive index measurements may be rather similar to those for Asian dust) [e.g., *Di Biagio et al.*, 2014a]. The modal radius and width of the single-mode distribution are prescribed from volume effective radius and width for the coarse mode (for radii $> 0.6\,\mu m$) of AERONET size distributions (http://aeronet.gsfc.nasa.gov) [*Dubovik et al.,* 2002]. Note that we use AERONET-derived radius and width averaged over East Asia observed during the dust outbreak case study described in section 4. According to test cases presented by *Pierangelo et al.* [2004] and *Vandenbussche et al.* [2013], IASI thermal infrared spectra are expected to be significantly sensitive to dust altitudes and AODs, as brightness temperatures may differ by ~10 to ~12 K (depending on wave number) both for changes in the AOD at

Table 1. Main Inputs and Parameters for the Radiative Transfer Calculations Performed by AEROIASI

Input or Parameter of AEROIASI	Description or Source
Spectral micro-windows for fitting IASI measurements	831, 903, 907, 913, 957, 975, 979, 1100, 1118, 1155, and 1183 cm^{-1} (central wave numbers)
Angles of scattering into the line of sight of IASI	0°, 57°, 86°, 92°, 135°, and 180° (from nadir)
Number of integration intervals of the scattering source function	50 both in the azimuth and nadir directions
Modal radius of the dust model (from AERONET volume effective radius of the aerosol coarse fraction)	0.92 μm (number size distribution) 2.34 μm (volume size distribution)
Modal size standard deviation of the dust model (from AERONET, as the radius)	1.75
Refractive index of the climatological dust model	OPAC/GADS refractive index for mineral dust models
A priori dust vertical profile	Derived from scaled CALIOP extinction profiles (1–2 March 2008 over East Asia)
Temperature profile and first guesses of H_2O profile and surface temperature	ERAI reanalysis interpolated in time and space for each pixel

10 μm from 0.75 to 2.5 or in the dust altitude by 3 km. On the other hand, a lower sensitivity is found with respect to particle size, as brightness temperatures change considering two typical dust size distributions at most by ~1 K and ~2 K (both around 1100 cm^{-1}) for a dust layer respectively located at 1–2 km and 4–5 km. Similar results are found for the case analyzed in this paper (see section 2.2).

A unique first guess of dust vertical distribution (the same fixed profile for all pixels) is considered in the inversion, which is obtained from an average of CALIOP extinction vertical profiles for dust over East Asia (all available measurements identified as dust layers during the event of section 4), scaled to particle concentration units (in order to set an a priori AOD at 10 μm of 0.03). Forward simulations include surface emissivity from a global monthly IASI-derived climatology [*Zhou et al.*, 2011]. For each pixel, we use atmospheric temperature profiles and first guesses of surface temperatures and water vapor profiles from ERA-Interim (ERAI) reanalysis [*Dee et al.*, 2011] of the European Centre Medium-Range Weather Forecast (ECMWF), for which data assimilation limits eventual biases.

Radiative transfer calculations are performed for each iteration using the line-by-line Karlsruhe Optimized and Precise Radiative transfer Algorithm (KOPRA) [*Stiller et al.*, 2000, 2002] accounting for light absorption, emission, and single scattering by aerosols based on a layer-by-layer approach [*Höpfner and Emde*, 2005]. As for relatively weak scattering particles [*Höpfner and Emde*, 2005], we do not expect significant errors in the simulated spectra when neglecting multiscattering of thermal infrared radiation by dust. Nonsphericity effects of dust-like particles are also likely negligible in the thermal infrared according to simulations of *Yang et al.* [2007], showing brightness temperature differences in the radiative signatures for spheroids and spheres below ~1 K. Dust optical properties are derived at each wavelength of the simulated spectra, using the climatological desert dust model and a Mie code [implemented by *Metzig*, 1984] and using optimizations from *Deirmendjian et al.* [1961] and *Kerker* [1969]. Scattering calculations account for radiation scattered into the line of sight of IASI that comes from six nadir angles (listed in Table 1), and spherical integrations are done over 50 intervals for both the azimuth and nadir directions. The simulated spectra account for absorption by water vapor (i.e., both the continuum and the absorption lines). The vertical grid of all profiles in the simulations is set between the surface and 12 km of altitude asl (above mean sea level), with 1 km increments. AEROIASI uses calibrated level 1C IASI data (from http://www.pole-ether.fr) from 12 micro-windows in the atmospheric window between 8 and 12 μm, which are merged into a measurement vector $y_{AEROIASI}$ (the list of micro-windows is given in Table 1). These micro-windows are chosen following a criterion of maximum information content [as classically done for trace gases and temperature by, e.g., *Rodgers*, 2000; *Worden et al.*, 2007]. This approach maximizes the information provided on the dust vertical profile, while minimizing the sum of the retrieval errors due to measurement noise, vertical smoothing, and systematic errors associated to the uncertainties of other variables (i.e., surface and atmospheric temperatures and the concentrations of H_2O, CO_2, O_3, NH_3, HNO_3, HCOO, CFC-11, CFC-12, and CH_3OH). The selected micro-windows are spectrally narrow (i.e., with typical micro-window widths spanning from 1 to 6 cm^{-1}), only including wavelengths with very low absorption by water vapor (i.e., in between H_2O absorbing lines) and excluding the absorption lines from other trace gases. The exclusion of these absorption lines is favored by the ultrafine spectral resolution of IASI spectra (i.e., 0.5 cm^{-1} after convolution by the instrument response function and sampling interval of 0.25 cm^{-1}). The spectral noise of IASI in these micro-windows ranges from 20 to 30 $nW/(cm^2\,cm^{-1}\,sr)$. Using thermal infrared measurements, AEROIASI retrievals are mostly sensitive to

coarse aerosols (with radii roughly greater than ~1 μm). Indeed, Mie calculations using OPAC dust refractive indices suggest that the contribution of fine dust particles (with radii $<$ ~1 μm) to total AODs at 10 μm is expected to be less than ~10% when using climatological desert dust size distributions [e.g., *Pierangelo et al.*, 2005] and below ~2% when accounting for particle size distributions of an Asian desert dust storm measured by *Clarke et al.* [2004].

For each IASI pixel, the AEROIASI retrieval scheme fits simultaneously all variables included in the following state vector x_{AEROIASI}:

$$x_{\mathrm{AEROLASI}} = \left[x_{T_s}^T \quad x_{\log(\mathrm{Ndust})}^T \quad x_{\mathrm{H_2O}}^T\right]^T \tag{1}$$

Thus, the vertical profile of dust x_{Ndust} is obtained while concurrently adjusting the corresponding surface temperature x_{T_s} and the water vapor mixing ratio profile $x_{\mathrm{H_2O}}$. Other variables, such as atmospheric temperature profiles, are not adjusted during the inversion. For avoiding negative results, the inversion procedure adjusts $x_{\log(\mathrm{Ndust})}$, which is the natural logarithm of x_{Ndust} (here in terms of number concentration in cm^{-3}). We use x_{Ndust}, a Mie code and the desert dust model for deriving the aerosol extinction profiles for each iteration and wavelength of y_{AEROIASI}.

When deriving x_{AEROIASI}, a Newtonian iteration process is used to account for the nonlinearity of the atmospheric radiative transfer [*Rodgers*, 2000; *von Clarmann et al.*, 2003]. AEROIASI also uses an auto-adaptive Tikhonov-Phillips-type [*Tikhonov*, 1963] altitude-dependent regularization. This method is conceived to avoid unrealistic oscillations in the retrieved dust profiles while adapting the results to the amount of information provided by the IASI measurements. For x_{H2O}, we consider the regularization strengths used by *Cuesta et al.* [2013], only allowing moderate adjustments [at most by 10%, with ~0.1 degrees of freedom (DOF)—calculated following *Steck*, 2002]. Therefore, the adjusted water vapor profiles remain within the uncertainties of the meteorological reanalysis used as first guesses. On the other hand, surface temperature is only slightly constrained (accounting for ~0.9 DOF), and it is adjusted using the differences in its spectral signature with respect to that of dust (see section 2.2). In the case of $x_{\log(\mathrm{Ndust})}$, the regularization constrains the zeroth and first derivatives of the retrieved profiles, with respect to a priori values (i.e., the first guesses of x_{AEROIASI}). Based on numerical simulations, the constraint strengths have been empirically chosen [following the general approach of *Kulawik et al.*, 2006] with weaker (stronger) constraints at the lower (upper) troposphere, for providing more adaptability in the atmospheric layer with higher aerosol variability. Moreover, the constraints of $x_{\log(\mathrm{Ndust})}$ are automatically scaled during the iterative procedure by implementing a Levenberg-Marquardt-type damping. This method uses a criterion for releasing (enhancing) the constraints when converging to lower (diverging to higher) root mean squared (RMS) differences between measured and simulated spectra. The scaling factor γ_i is updated at each iteration i according to the following expression:

$$\gamma_i = \left(\mathrm{RMS}_{i-1}/\mathrm{RMS}_{i-2}\right)^k \tag{2}$$

with k set empirically to a value of 0.3 in order to ensure numerical stability. The maximum number of iterations is empirically set to 15 (beyond which the state vector varies at most by 5%). The convergence criterion is based on the relative minimum of the spectral residuals (used as proxy for the variation of the cost function) along the iterations. The absolute value of the spectral residuals is checked in a second step (i.e., quality assurance checks; see below).

The overall results of AEROIASI show that the DOF or the number of independent pieces of information in the retrieval of dust profiles varies during the iterative procedure, a typical value of ~1.4 being used during the first iterations designed to determine the shape of the dust extinction profiles. This is similar to the DOF of ~1.5 obtained with the approach of *Vandenbussche et al.* [2013], which also derives dust vertical profiles from IASI. In order to obtain numerically stable results, DOFs are limited to ~1 during the last iterations near convergence (using the auto-adaptive scaling factor γ). Lower DOF values are usually obtained for low aerosol loads (typically for AOD below ~0.2). As the DOF of the AEROIASI dust retrieval are less than 2, the approach mainly allows describing the vertical distribution of a single aerosol layer, with expected correlation between the points of the retrieved dust profile. Moreover, we note the retrievals of dust columnar amount and dust vertical distribution are not entirely independent. Indeed, the iterative procedure for most pixels first adjusts the dust layer altitudes (in the first iterations) and then it modulates

the total AODs and the vertical profile shapes for minimizing the spectral residuals. Hence, AODs are conditioned by the dust layer altitudes initially obtained.

Once all IASI spectra are fitted, a series of quality checks are performed in order to screen out cloudy measurements and aberrant retrievals. We exclude IASI pixels with derived surface temperatures below their ERAI reanalyses counterparts by more than 15 K, RMS spectral residuals above 140 nW/(cm^{-1} cm^2 sr), or pixels exhibiting too high horizontal variability with respect to their closest 5 pixels (using a threshold of 500 particles m^{-2} for the standard deviation of the vertically integrated particle number concentration). Quality-checked AEROIASI retrievals are obtained for 95% of cloud-free pixels over both land and ocean (as identified from IASI level 2 cloud retrievals for the 1–3 March 2008 period, over East Asia). As spectral residuals (from uncertainties, e.g., in the dust climatological model and temperature) are usually larger than IASI spectral noise, we determined the threshold of 140 nW/(cm^{-1} cm^2 sr) from the histograms of spectral residuals for cloudy and cloud-free pixels. Little overlap is seen between these histograms, as pixels with optically dense clouds exhibit spectral residuals below this threshold only in 3% of the cases (i.e., 97% of confidence for detecting dense clouds). On the other hand, subvisible cirrus clouds (with optical depths below ~0.02) may be difficult to screen out, as their radiative signature may be a slight attenuation of the radiation emitted by the surface, as spectrally smooth as for aerosols (which could be undetected by the cloud filters listed above).

Final AEROIASI outputs are calculated with a Mie code, using x_{Ndust} and the desert dust model. For each pixel, we derive a vertical profile of dust extinction coefficient ($\alpha_{10\,\mu\mathrm{m}}$ in km^{-1}) at 10 μm, the associated AOD (by vertical integration of the extinction profile), and mean and top altitudes of the observed dust layer. The mean altitude of the observed dust layer is defined as the altitude below which the integral of the extinction coefficient profile reaches 50% of the AOD. Likewise, the altitude of the top of the dust layer is defined as the altitude below which the integral of the extinction coefficient profile reaches 95% of the AOD. Indeed, AEROIASI provides valuable information not only on the mean altitude of the dust layers but also on their vertical extent (i.e., layer top heights and whether the layers reach the ground or are elevated). In the next sections, these dust layer altitudes are provided for AODs at 10 μm above 0.2, as greater ambiguities in the determination of these altitudes arise for low dust loads. Note that this is not the case for AEROIASI retrievals of dust vertical extinction profiles, which are presented in the next sections for most (95%) cloud-free IASI pixels. In the following, AEROIASI retrievals of dust layer altitudes and aerosol extinction profiles are validated against CALIOP retrievals (see section 2.3), while AEROIASI retrievals of AOD are validated against AERONET retrievals (see section 2.4).

2.2. Sensitivity Analysis of AEROIASI Retrievals

Figure 2 illustrates the spectral effects of desert dust on IASI thermal infrared measurements and the dust optical properties calculated for the spectral micro-windows used for AEROIASI. We compare five simulated spectra for the following: (i) a pristine case, (ii) a low-level dust layer [extending from the ground to 2.3 km above ground level (agl)] with an AOD of 0.6, (iii) an elevated dust layer (extending from 2 to 4.3 km agl) with an AOD of 0.6, (iv) an elevated dust layer with an AOD of 1.2, and (v) a low-level dust layer with an AOD of 0.6 but with a surface temperature reduced by 3 K with respect to (ii). Figure 2b shows significantly distinct spectral signatures corresponding to changes in the AOD (in red), the dust vertical distribution (in light blue), or the surface temperature (in yellow). Considering three parts of the spectrum delimited between 800, 910, 1050, and 1200 cm^{-1}, the spectral slopes of the changes in radiation are different in sign for the three variables (Figure 2b). For a given AOD, colder dust layers (i.e., the case of the elevated dust layer) emit less radiation, resulting in a decrease of the radiance. This radiance reduction is more significant around 800 and 1050 cm^{-1} but less near 910 and 1200 cm^{-1} as seen in Figure 2b (light blue). Besides, an increase in AOD produces a decrease in the radiances (red curve in Figure 2b) that is greater for higher radiance values (see Figure 2a), as expected due to the corresponding reduction in atmospheric transmission. Dust attenuates thermal infrared radiation due to both absorption and scattering. The absorption AOD (AAOD) accounts for approximately half of the AOD, except between 1150 and 1200 cm^{-1} (where the AAOD is ~90% of the AOD; see Figure 2c). Between 950 and 1150 cm^{-1}, a band of greater AOD and AAOD is apparent, which is linked to a significant increase in the imaginary and real parts of the complex refractive index of dust [see, e.g., *Di Biagio et al.*, 2014a, 2014b]. Note that the retrieval does not use IASI measurements from the strongest Si-O vibrational absorption bands near 1050 cm^{-1} and there is only one AEROIASI micro-window near the quartz resonant peak around 1183 cm^{-1} [where radiative

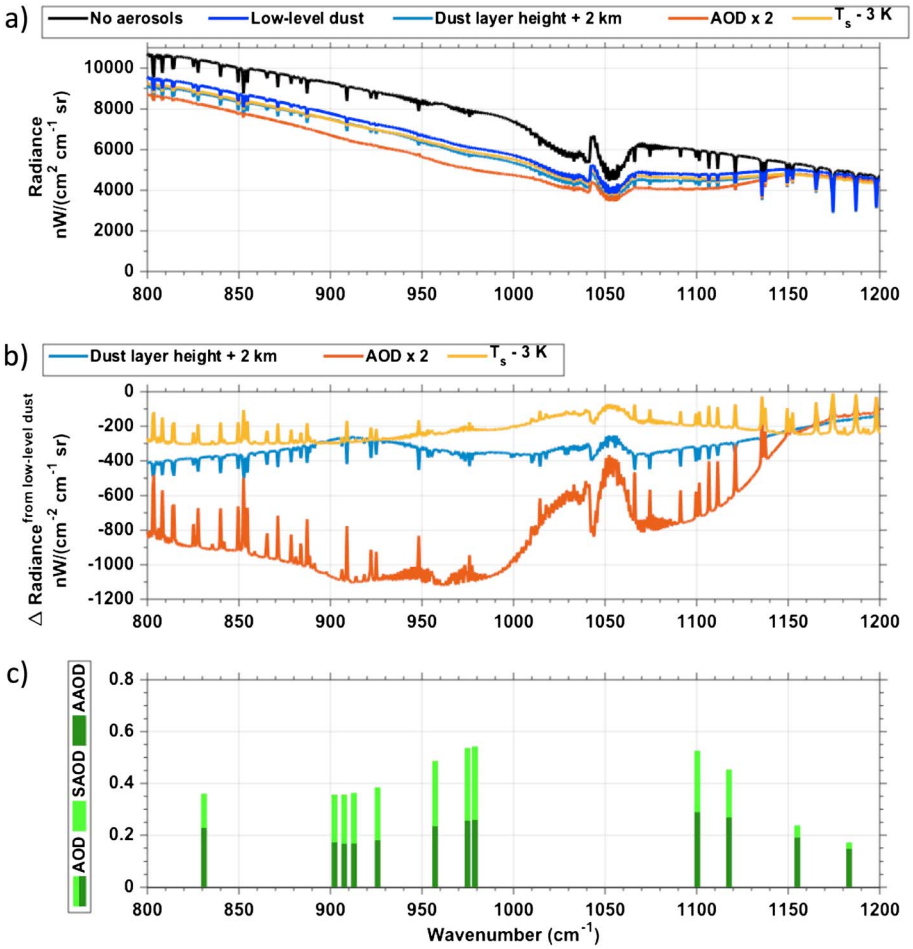

Figure 2. (a) IASI-like spectra simulated from 800 to 1200 cm^{-1} in the thermal infrared for five atmospheric scenes: a pristine case, a low-level dust layer reaching the surface with an AOD at 10 μm of 0.6 (the profile is shown in Figure 3e) and the same dust layer but (i) elevated 2 km higher, (ii) with an AOD twice as high, or (iii) with a surface temperature reduced by 3 K. (b) Differences of the IASI spectra when the dust layer is 2 km higher (light blue), the AOD twice as high (red), and T_s minus 3 K (yellow), with respect to low-level dust case (blue in Figure 2a). (c) AOD, AAOD (absorption AOD), and SAOD (scattering AOD) for the case of lower AOD in Figure 2a calculated at the spectral micro-windows used for the AEROIASI retrieval.

signatures of nonsphericity and fine dust particles may be more significant, according to, e.g., *Legrand et al.*, 2014]. On the other hand, spectral signatures from changes in surface temperature are different from those associated to dust, showing a single change in slope near 1050 cm^{-1} (yellow in Figure 2b).

Additionally, sensitivity of radiances in the AEROIASI spectral micro-windows with respect to particle size (for modal radii ±10%, considering the case of Figure 2) is found to be a factor ~10 and ~4 lower than those induced by respectively an increase in AODs by a factor 2 (red curve in Figure 2b) and an increase in dust altitude of 2 km (light blue curve in Figure 2b). Similar results are obtained using high spectral resolution refractive indices estimated by *Di Biagio et al.* [2014a] for dust from China. Moreover, the spectral signature of several gases absorption lines (i.e., spikes in the spectra) are also different for the four dusty cases (although this effect is negligible for the spectral micro-windows of AEROIASI).

Figures 3e–3p and Table 2 present sensitivity analyses of AEROIASI retrievals with respect to the considered dust model (i.e., particle size and the refractive index) and main inputs of the method (i.e., surface and atmospheric temperatures as well as a priori particle and H_2O concentrations; Figures 3a–3c). For this, we analyze the variability of AEROIASI results when perturbing the values of each of method's inputs. We use IASI data for two typical atmospheric conditions: a low-level dust layer reaching the ground and an elevated dust layer, both observed on 2 March 2008 (40 pixels with rather homogenous results for each

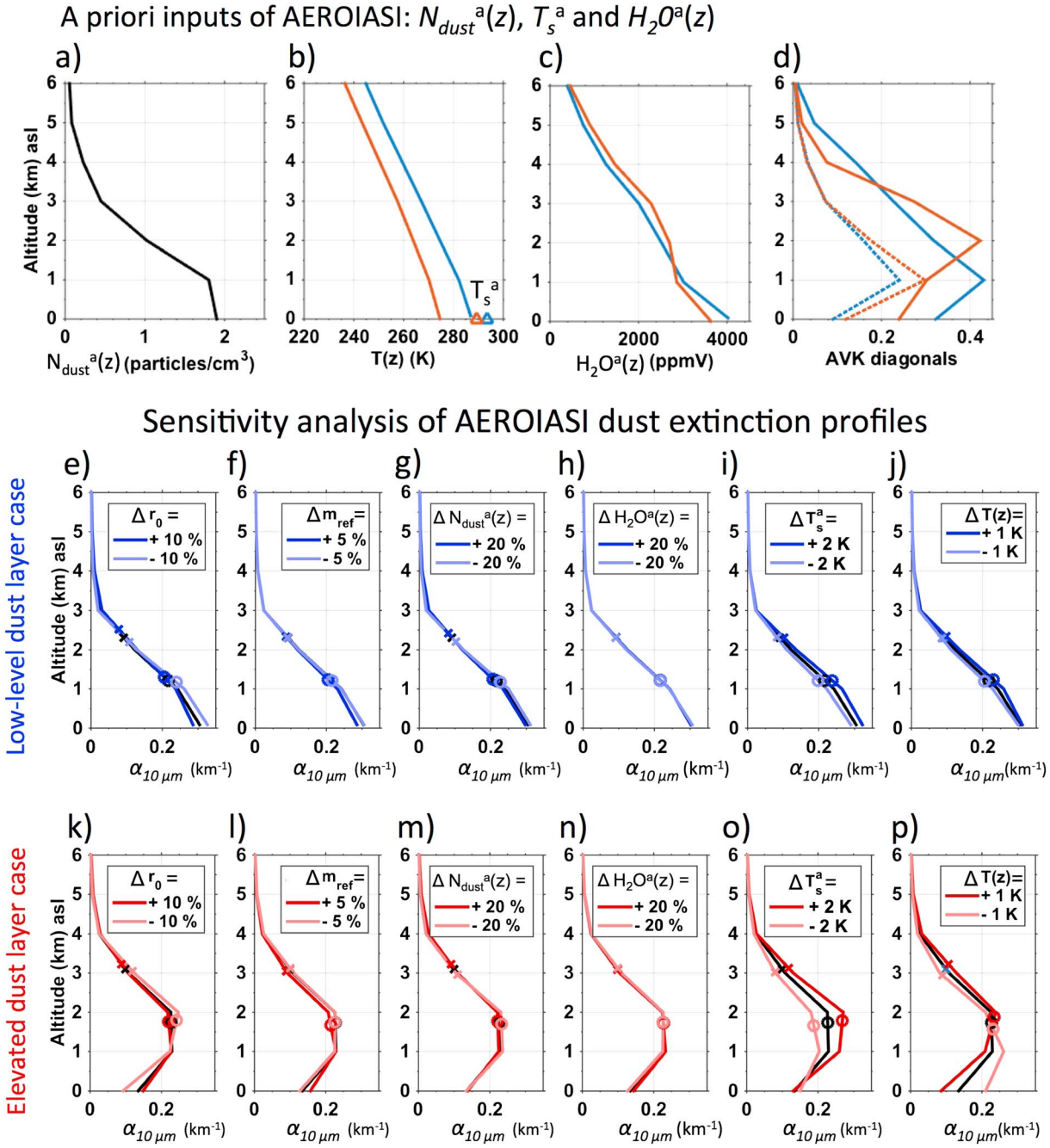

Figure 3. (a) A priori dust number concentration profile for AEROIASI, (b) mean temperature profiles (lines) and surface temperatures (triangles at the surface) used in AEROIASI, (c) mean a priori H_2O profiles, and (d) diagonals of the averaging kernels on the first (dotted lines) and second (solid lines) iterations for examples of AEROIASI dust profile retrievals for the two cases of the sensitivity analysis: a low-level dust layer (blue) and an elevated one (red). Sensitivity of AEROIASI-derived dust vertical profiles ($\alpha_{10\,\mu m}$ shown in Figures 3e–3p) with respect to perturbations (indicated in the legends by Δ) in the following inputs: (e and k) the dust modal radius, (f and l) the dust refractive index, (g and m) the a priori dust profile, (h and n) the a priori H_2O profile, (i and o) the a priori surface temperature, and (j and p) the temperature profiles. Figures 33e–33j and 3k–3p respectively correspond to the low-level and elevated dust cases mentioned above, respectively shown in blue and red for perturbed retrievals and in black for unperturbed results. See Table 2 for more details on the sensitivity analysis. The vertical locations of the circles and crosses in Figures 3e–3p indicate respectively the retrieved mean and top altitudes of the dust layers.

case). The results show that AEROIASI retrievals are no very sensitive to the dust model parameters and the a priori profiles of dust and H_2O (below 5% for the AOD and at most 10% to 14% for the dust layer heights; Figures 3e, 3k, 3h, and 3n and Table 2), while moderate sensitivity is seen with respect to the uncertainties of atmospheric and surface temperatures (at most between 17% and 29%; Figures 3j, 3p, 3i, and 3o).

Table 2. Sensitivity Analyses of AEROIASI With Respect to the Climatological Dust Model and the A Priori Inputs[a]

	Mean Variability of AEROIASI Retrievals (Standard Deviation/%)					
	Low-Level Dust Layer			Elevated Dust Layer		
Perturbed Variable	AOD 10 μm	Mean Height (km)	Top Height (km)	AOD 10 μm	Mean Height (km)	Top Height (km)
Modal radius +/− 10%	0.03/4.3%	0.13/10%	0.33/14%	0.01/1.2%	0.03/1.8%	0.18/5.7%
Refractive index +/− 5%	0.02/4.0%	0.02/1.6%	0.03/1.1%	0.02/3.5%	0.07/2.4%	0.08/4.5%
A priori dust profile +/− 20%	0.01/2.3%	0.22/9.4%	0.07/6.1%	0.002/0.3%	0.07/4.1%	0.26/8.4%
A priori H_2O profile +/− 20%	0.002/0.4%	0.01/0.6%	0.01/0.3%	0.01/1.1%	0.04/2.0%	0.04/1.3%
A priori surface temp. +/− 2 K	0.09/16%	0.001/0.1%	0.01/0.3%	0.20/29%	0.12/7.2%	0.10/3.3%
Temperature profile +/− 1 K	0.06/12%	0.03/2.6%	0.06/2.4%	0.02/3.7%	0.29/17%	0.28/9.2%

[a]Two typical observing scenes are considered: a low-level dust layer reaching the ground (with 0.53 of AOD at 10 μm, mean and top layer heights of 1.22 and 2.31 km agl, respectively) and an elevated dust layer (with 0.67 of AOD at 10 μm, mean and top layer heights of 1.74 km and 3.10 km agl, respectively). For each scene, we analyze the average of AEROIASI retrievals for 40 adjacent pixels (that show very similar results). The low-level and elevated dust layer scenes correspond to real data sets of 2 March 2008 respectively from 30–32°N 112.5–115°E and 38–40°N 119–121.5°E. Refractive indices are perturbed by changes in both the real and imaginary parts by +/− 5%.

Indeed, we expect an influence of the a priori knowledge of temperature on the precision of AEROIASI, as the approach is based on the analysis of thermal radiation. These tests also suggest that the sensitivity of AEROIASI is higher for the case of the elevated dust layer (also with lower atmospheric temperatures; see Figure 3b) than for dust layers reaching the ground. This is probably linked to the lower temperature of the elevated dust layer (due to the altitude of the layer and atmospheric temperature itself) that emits weaker radiation, than for the warmer layer closer to the ground with a stronger emission signature on IASI spectra.

Figure 3 also illustrates the ability of AEROIASI to derive dust profiles. In the two cases, the retrievals exhibit higher AODs (a factor ~20) and different dust layer altitudes with respect to the a priori (roughly 1 km below or above respectively in the low-level and elevated dust layers). According to averaging kernel calculations [following *Steck*, 2002], AEROIASI sensitivity during the first iterations (dotted lines in Figure 3d) shows Gaussian-like vertical distributions, peaking around 1 km and extending from the surface up to 4–5 km. This provides a good flexibility for obtaining a reasonable variety of retrieved profiles (e.g., low-level or elevated dust layers at different altitudes and variable thicknesses). In the following iterations, AEROIASI averaging kernels are slightly narrower and vertically shifted toward the mean altitude of the layer (solid lines in Figure 3d), during which it mainly fits the AOD. Besides, surface temperatures adjusted by AEROIASI for regions with high dust loads are typically consistent with reductions by a few degrees with respect to those of the ERAI reanalyses (which do not directly account for dust radiative effects on surface temperature).

2.3. Validation of Dust Vertical Profile Retrieval From AEROIASI

Based on observations of a dust outbreak over East Asia on 1 and 2 March 2008 (the documented case study detailed in section 4), we analyze the information on dust vertical distribution derived from AEROIASI by comparison with individual transects of aerosol extinction vertical profiles from the CALIOP spaceborne lidar. For this, CALIOP level 1 measurements (from http://www.icare.univ-lille1.fr) of attenuated backscatter profiles are inverted using a classical approach [*Fernald et al.*, 1972; *Fernald*, 1984] in order to correct for atmospheric transmission. Following *Cuesta et al.* [2009], we use a climatological particle backscatter-to-extinction ratio of $0.024\,sr^{-1}$ for dust particles [*Cattrall et al.*, 2005], which is vertically modulated by a multiple scattering coefficient according to *Young et al.* [2008]. Multiple scattering is accounted for in order to avoid unrealistic large extinction coefficient values near the surface, as is often the case for dense dust layers. As CALIPSO overpasses are at around 0130 and 1330 LT and IASI at 0930 and 2130 LT, we compare the closest time coincidences between the two types of observations. We do not conduct comparisons with AEROIASI measurements precisely located along a CALIOP transect, but instead, we try to account for horizontal drift of air masses between the times of the overpasses (3 to 6 h). The locations of the IASI pixels to be compared with the CALIOP observations are estimated using average wind speeds and directions from ERAI reanalysis at the two extreme points of the CALIOP transects and the mean altitudes of the dust layers. Moreover, AEROIASI transects are obtained from the horizontal moving

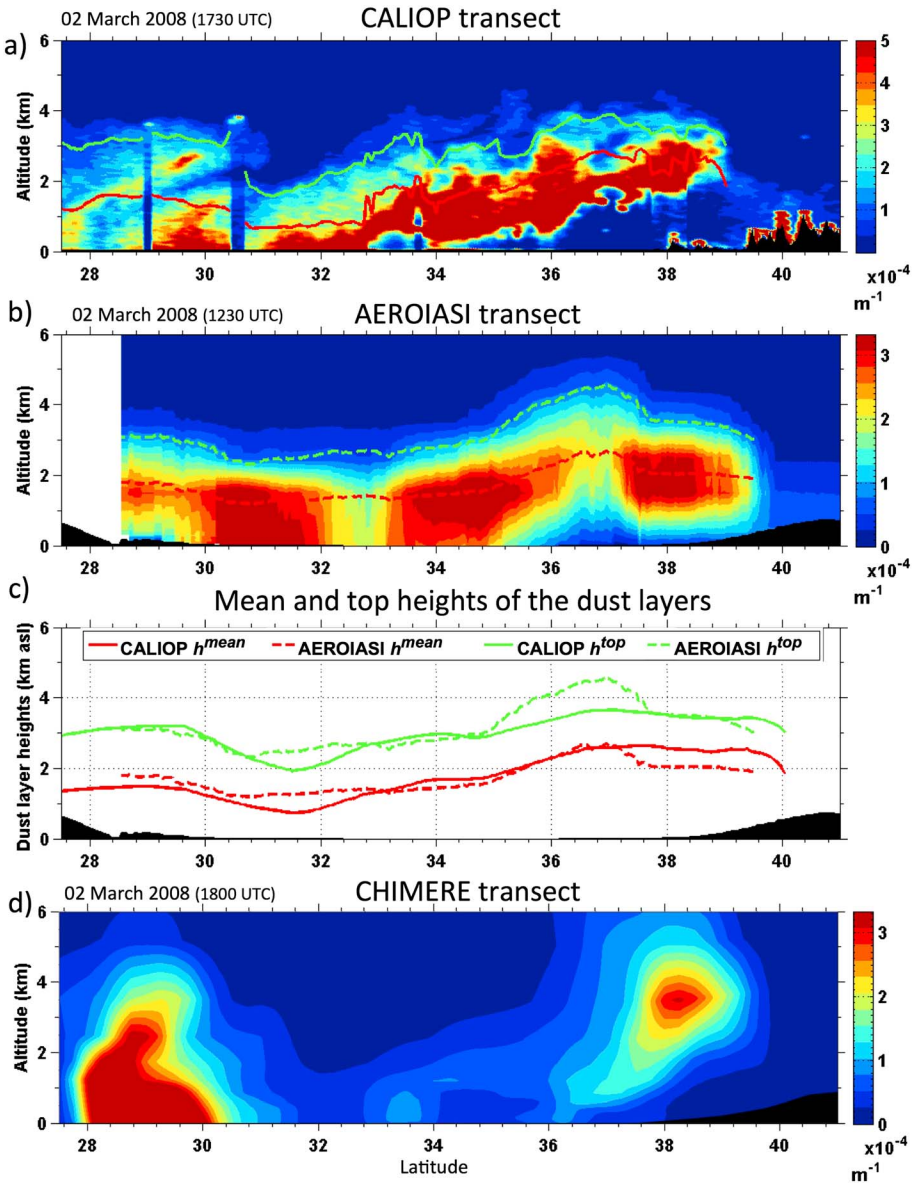

Figure 4. Transects of vertical profiles of aerosol extinction coefficient (m^{-1}) from (a) CALIOP spaceborne lidar at 532 nm on 2 March 2008 at 1730 UTC and (b) AEROIASI at 10 μm on 2 March at 1230 UTC, colocalized accounting for the average wind from ERAI reanalysis and moving average over ±1°, mostly over the Yellow Sea. Figure 4c shows mean (red) and top (green) altitudes of the dust layers from CALIOP (plain lines, here applying a moving average of 2° of latitude for consistency with AEROIASI) and AEROIASI (dashed lines) derived using the same criteria. (d) CHIMERE transect of dust extinction profiles at 550 nm colocated with the CALIOP track of Figure 4a.

average of all available retrieved profiles (vertically interpolated every 100 m) for pixels within 2° (±1°) of latitude/longitude from the location of each CALIOP profile.

Figures 4 and 5 show comparisons between AEROIASI and CALIOP colocated transects (altitude vs. latitude) of particle extinction coefficient profiles at 10 μm and 532 nm, respectively. Three example cases are shown, one corresponding to elevated dust layers mostly over the Yellow Sea on 2 March (Figure 4) and two other cases of dust extending from the surface up to a few kilometers above the ground over continental China on 1 and 2 March (Figure 5). A very good agreement between AEROIASI and CALIOP transects is obtained, both in terms of the dust layer vertical distribution and their horizontal location along the CALIPSO track. In Figure 4, both AEROIASI and CALIOP show a dense dust layer reaching the surface between 30°N and 32°N, near the ground but slightly elevated at 34°N and ascending northward up to similar altitudes (mean

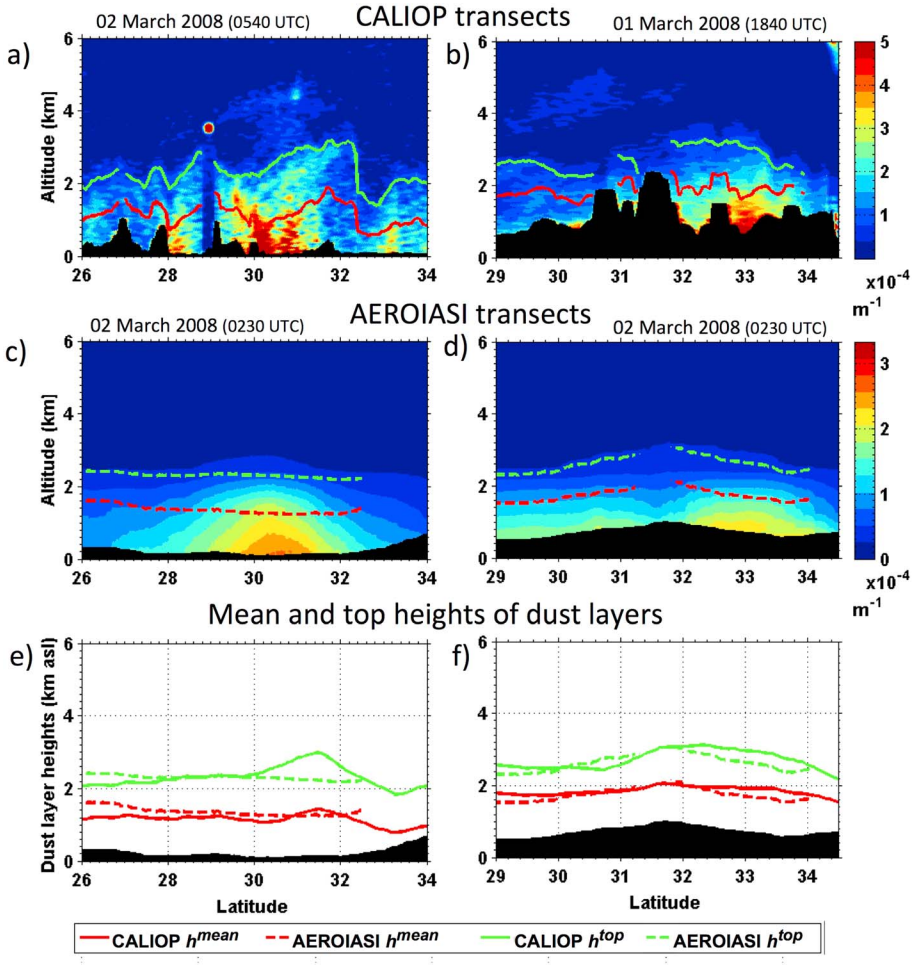

Figure 5. Same as Figure 4 but for CALIPSO overpasses on 2 March 2008 (a) at 0540 UTC and (b) on 1 March 2008 at 1840 UTC. (c and d) AEROIASI transects colocated with CALIOP observations, both derived from IASI measurements of 2 March 2008 at 0230 UTC. (e and f) Comparisons of the dust layers mean and top altitudes for the CALIOP transects respectively in Figures 5a and 5b.

altitudes around 2.5 km agl) while being detached from the surface from 35°N to 38°N. Around 29°N, an elevated southern dust plume not reaching the ground is as well captured by both instruments. The two cases of dust layers reaching the ground shown in Figure 5 are also similarly described by AEROIASI and CALIOP. Both instruments show a deeper layer on 2 March reaching ~2.4 km agl on average (mean altitude of ~1.2 km agl) and a shallower layer on 1 March up ~1.8 km agl (mean altitude of ~0.8 km agl), with all dust layers reaching the ground. More details on the interpretation of these data will be provided in section 4.

Quantitative comparisons for the mean (red lines) and top (green lines) altitudes of the dust layers derived by CALIOP and AEROIASI are shown in Figures 4c, 5e, and 5f, and the corresponding statistics are given in Table 3. The mean and top altitudes of the dust layers are defined similarly for IASI and CALIOP (see section 2.1). For consistency, a moving average of 2° of latitude (~200 km along the track) is applied for CALIOP-derived altitudes. In the upper troposphere, AEROIASI-derived profiles often show systematic errors associated with the shape of the a priori dust profile, which correspond to an AOD of ~0.02. As this uncertainty may cause noisy detections, the layer top altitudes are estimated without accounting for the topmost 0.02 of AOD in the vertical integration of both AEROIASI and CALIOP profiles. A good quantitative agreement can be noted, with low mean biases for both altitudes of about ~100 to ~150 m, considering both individual CALIPSO tracks and averaging the three cases (see Table 3), and RMS differences of about ~250 m and ~350 m for the mean and top altitudes, respectively. The changes in the dust layer altitudes

Table 3. Comparison of Mean and Top Altitudes of Dust Layers Derived From AEROIASI and CALIOP Extinction Coefficient Profiles, for Three Transects Over East Asia Between 1 and 2 March 2008[a]

	Mean Heights of Dust Layers			Top Heights of Dust Layers		
Case	Bias (km)	Correlation	RMS (km)	Bias (km)	Correlation	RMS (km)
Elevated layer on 2 March	0.01	0.95	0.30	0.20	0.92	0.40
Deeper low-level layer on 2 March	0.15	0.33	0.21	−0.10	−0.89	0.33
Shallow low-level layer on 1 March	−0.14	0.87	0.17	−0.16	0.86	0.23
All cases (asl)	0.03	0.94	0.26	0.04	0.91	0.35
All cases (agl)	0.11	0.96	0.28	0.13	0.94	0.37

[a]Mean and top altitudes are obtained as those with 50% and 95% of AOD below. Biases in heights are calculated as AEROIASI minus CALIPSO altitudes.

highlighted by AEROIASI agree very well with those seen by CALIOP (e.g., see the evolution along the transect in Figure 4), with high linear correlation coefficients of ~0.95 when considering data sets with significant changes in the altitudes of the dust layers (i.e., the case of elevated layers of Figure 4 and for all cases). These results indicate that AEROIASI reliably depicts the vertical distribution of the main dust layers, in agreement with CALIPSO. However, fine structures and multiple layers can only be observed with CALIOP (e.g., more dust closer to the surface at 30–32°N in Figure 4a or a deeper layer at 32°N in Figure 5a). Some of the differences seen between the CALIOP and AEROIASI measurements are also likely related to the evolution (between the satellite overpasses) of the vertical distribution of the dust layers due to vertical motion, which is not accounted for in the analysis. Moreover, the AEROIASI-derived dust profiles do not show apparent losses of sensitivity in the lower atmospheric layers for the range of AOD values at 10 μm analyzed in this section (~0.15 at 29–31°N in Figure 5d and ~1 at 34–35°N in Figure 4b). It is also worth noting that for AODs at 10 μm of 1, total atmospheric transmission for some spectral micro-windows of AEROIASI may remain relatively high (e.g., 0.6 at 831 cm^{-1}).

2.4. Validation of the Dust Optical Depth From AEROIASI Over East Asia

In order to assess the quality of the AEROIASI dust-related AOD retrievals over East Asia, we compare them with AOD measurements from the AERONET ground-based sun photometer network [*Holben et al.*, 1998]. We consider 13 sites over East Asia (see Figure 6b) for the period from March to September 2008 (see examples of time series in Figure 6c). Significant contributions of desert dust from the Mongolian and Chinese deserts are expected during these months of the year [e.g., *Laurent et al.,* 2006]. For consistency, the comparison is done between AOD from AEROIASI retrieved at 10 μm (mainly sensitivity to coarse particles) and extrapolated to 500 nm using an Angström exponent of 0.28 (derived from the climatological desert dust model, which accounts for absorptive differences in the spectral regions), and AERONET measurements of the so-called "coarse mode" AOD at 500 nm. The latter ones are derived using the approach of *O'Neill et al.* [2003] for separating the contributions of the fine and coarse modes based on the AOD spectral dependency (coarse mode AOD for the 13 sites is available as level 1.5 data from http://aeronet.gsfc.nasa.gov). The criteria of spatiotemporal coincidence are ±30 min and ±1° of latitude and longitude. In order to ensure comparison in cloud-free conditions, we only consider AERONET AOD observations with a temporal variability less than 20% within ±1 h. Furthermore, we impose that a minimum of 10 quality-checked IASI pixels and 2 AERONET measurements be available per item of the comparison. After all outliers have been removed from the time series, AEROIASI and AERONET retrievals are averaged in order to provide daily averages and to allow for comparison over land and over sea (if AERONET stations are close to the coast).

The comparison between the AOD derived from AEROIASI and AERONET shows a good overall agreement (Figure 6a and Table 4). Considering all available items (a sample of 625 measurements), the mean bias is very low (less than 1%), the linear correlation R is high (0.79), and the RMS difference between AODs is ~0.10. The correlation and RMS difference are similar to those derived from comparisons conducted using AOD retrievals obtained from other IASI-processing methods [e.g., *Klüser et al.,* 2012]. AEROIASI variability is close to that of AERONET (the ratio between AEROIASI and AERONET standard deviations is 0.89). Furthermore, very similar results are obtained over all AERONET stations located between 110°E and 125°E (a sample of 404 measurements), with a very weak mean bias (<0.001), the same RMS, and moderately

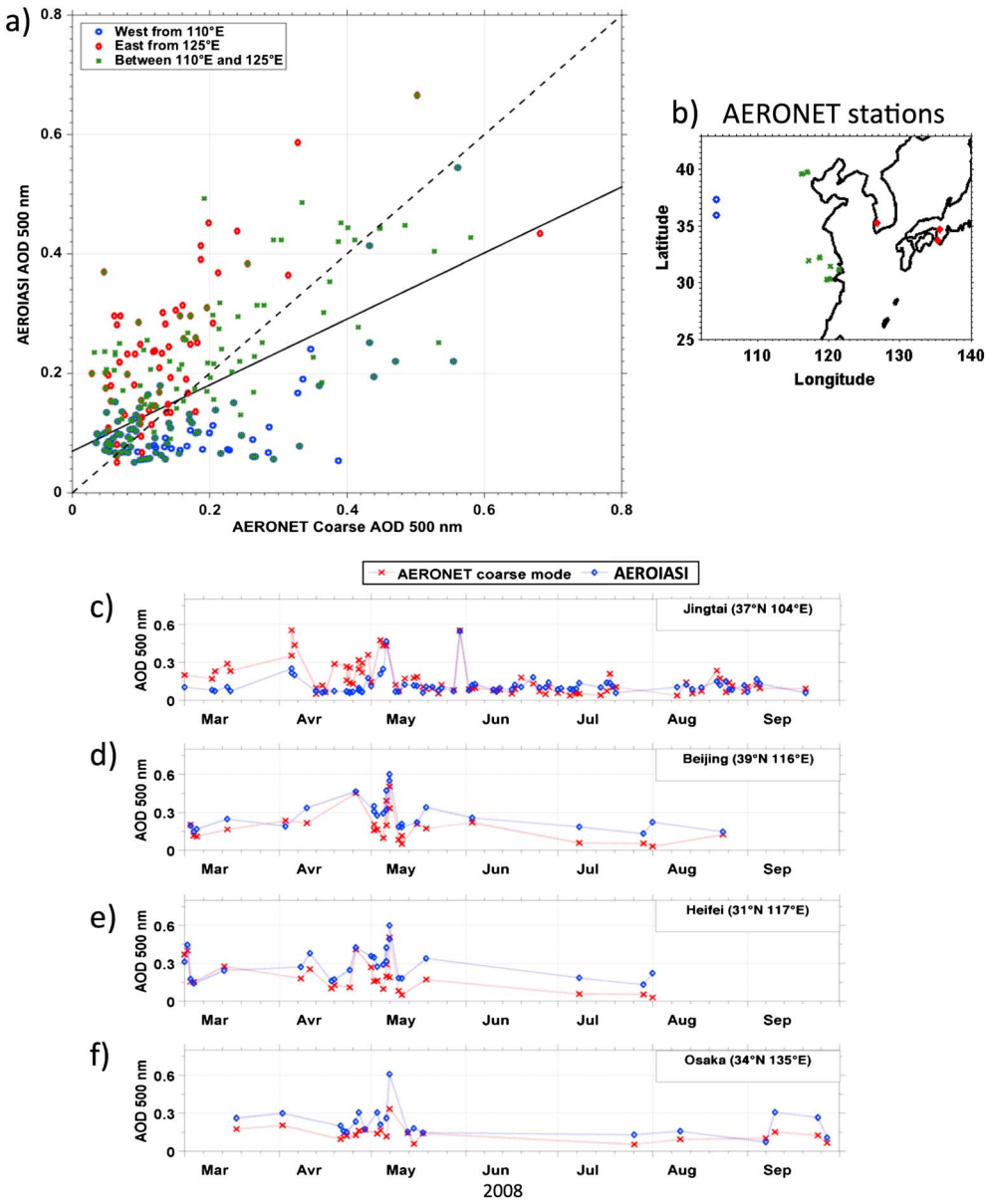

Figure 6. Comparison of aerosol optical depth (AOD) from AEROIASI (extrapolated to 500 nm) and coarse mode AOD at 500 nm measured from 13 AERONET sun photometer sites over East Asia, between March and September 2008: (a) scatterplot of all 625 measurements in the comparison (the linear regression of all measurements and the 1:1 line are indicated respectively as solid and dashed black lines), (b) locations of 13 AERONET sites over East Asia, and examples of time series of daily AOD for four AERONET sites, at (c) Jingtai (northwestern China), (d) Heifei (central-eastern China), (e) Beijing (northeastern China), and (f) Osaka (Japan).

higher linear correlation (0.82) between the AOD retrievals. West of 110°E and east of 125°E, relatively high linear correlations are also highlighted. Furthermore, RMS values similar to those derived for the whole data set are obtained. However, regional biases are detected, with an overestimation (~0.1 on the AOD) far away from desert dust sources (i.e., east of 125°E, at least ~2000 km away) and an underestimation (~0.04 on the AOD) closer to dust sources, i.e., west of 110°E. These biases are likely linked to the desert dust model used in AEROIASI, in which aerosol size distributions are derived from the available AERONET measurements (mostly from the stations comprised between 110°E and 125°E). Changes in the dust size distributions near the source regions and during long-range transport (e.g., by particle settling) and the presence of other coarse aerosols such as sea salt on the eastern region could induce the observed differences. We expect to reduce such regional biases by using different dust models for each region or

Table 4. Comparison of AEROIASI and AERONET Observations of AOD at 500 nm, for 13 Sun Photometer Stations Over East Asia, From March to September 2008[a]

Region	Mean Bias	RMS	Linear Correlation *R*	Standard Deviation Ratio	Number of Measurements
East Asia	−0.0005	0.10	0.79	0.89	625
West from 110°E	−0.04	0.10	0.82	0.61	154
From 110 to 125°E	−0.0006	0.10	0.82	0.88	404
East from 125°E	+0.097	0.13	0.82	1.18	67

[a]AOD from AEROIASI is retrieved at 10 μm and extrapolated to 500 nm. AOD from AERONET is the so-called "coarse mode" retrieval. These data sets are also presented in Figure 6. Biases in AOD are calculated as AEROIASI minus AERONET.

relaxing the initial constraint on the size distribution in the AEROIASI method, thus allowing to iteratively adjust the particle size distribution.

The AOD time series for four stations at short, moderate, and long distances from dust sources (Jingtai—western China, Heifei—eastern China, Beijing—northeastern China, and Osaka—Japan, respectively) shows the ability of AEROIASI retrievals to describe the daily evolution of the AOD due to coarse dust aerosols (Figures 6c–6f), both in the presence of dust events (timing and intensity) and for periods when the dust load in the atmosphere is small (background conditions). This is observed for day-to-day and seasonal variabilities. In some cases (particularly in Jingtai), AEROIASI is capable of observing daily AODs as low as 0.05, in agreement with AERONET. Linear correlation coefficients between AEROIASI and AERONET are significant, varying from 0.82 (at Jingtai) up to ~0.9 (at Beijing and Osaka) and reaching 0.92 (at Heifei). This is consistent with the higher regional linear correlations between AEROIASI and AERONET, as previously noted. The time series at Jingtai (west of China) shows that some of the AOD peaks are well reproduced (during May) and some are underestimated (in March and April). Good AOD tracking ability by AEROIASI (with a positive bias) is also seen at the Osaka station. The AOD RMS differences between AEROIASI and AERONET range between ~0.10 and ~0.12 for the four sites.

3. Other Data Sets

In addition to AEROIASI observations, other data sets are used in section 4 to describe the desert dust outbreak over East Asia during the 1–3 March 2008 period. In this section, we provide a brief description of each additional observational or modeling data set and how we use them.

3.1. MODIS Observations

MODIS observations of AOD at 550 nm derived with the Dark-Target approach are used for complementary descriptions of the horizontal aerosol distribution over East Asia. We consider MODIS level 2 products, so-called MOD04_L2 (from http://ladsweb.nascom.nasa.gov), with 10 km horizontal resolution and observed from the Terra satellite (with overpass at 1030 LT, thus ~1 h later than the IASI morning overpass). These data sets are used to verify the consistency of aerosol plume distributions with respect to AEROIASI-derived AOD at 10 μm. They are complementary, since MODIS-derived AOD at 550 nm is expected to be sensitive to both fine and coarse aerosols, whereas AEROIASI (in the thermal infrared) only to coarser desert dust.

3.2. CHIMERE Regional Model

Desert dust distribution over East Asia is also analyzed with numerical simulations from the CHIMERE regional chemistry-transport model [e.g., *Schmechtig et al.*, 2011; *Menut et al.*, 2013]. We use them to study the evolution of the different dust plumes observed during the case study described in section 4, by linking the emission region with the meteorological conditions leading to dust uplift and the transport. We also use CHIMERE to identify the dust plumes lifted over the northern Chinese deserts close to the Loess plateau, which is one of the two active sources of the case study of section 4. For this, dust emissions from the Gobi desert (the other active source) are switched off.

In our study, the CHIMERE model is ran over a large domain (21–47°N 74–149°E) covering all major dust source regions affecting East Asia, with a horizontal mesh size of 0.25° × 0.25°. Simulations are performed with an hourly time step, 15 vertical levels, and driven by ECMWF operational meteorological fields. The

only simulated species is desert dust. Dust concentration is initialized to zero, and a long spin-up time (5 days) is necessary to simulate realistic dust concentrations. Dust emission fluxes are calculated using the parameterization of *Marticorena and Bergametti* [1995] for saltation and the dust production model proposed by *Alfaro and Gomes* [2001] for sandblasting. Dust emission calculations use surface and soil up-to-date databases of roughness lengths derived from POLDER-1 surface products [*Laurent et al.*, 2005] as well as soil size distribution and texture obtained from in situ sampling [*Laurent et al.*, 2006] for the main Chinese arid areas. During transport, the 12-bin dust size distribution proposed by *Foret et al.* [2006] for appropriate representation of dust concentration and optical depth is used. AOD and extinction profiles from dust are calculated at 550 nm using Mie calculations with climatological refractive index for desert dust from *Moulin et al.* [2001]. These dust optical properties are used for qualitative comparisons with those derived from AEROIASI at 10 μm.

3.3. ERA-Interim Meteorological Reanalysis

Meteorological conditions leading to dust uplift and transport over East Asia are described in section 4 with ERA-Interim reanalysis [*Dee et al.*, 2011] produced by ECMWF. We use meteorological fields (from http://climserv.ipsl.polytechnique.fr) with global coverage, a horizontal resolution of $0.75° \times 0.75°$, 37 pressure levels, and a time step of 6 h (interpolated for other hours). Wind, geopotential height, and equivalent potential temperature fields describe the locations of a synoptic low-pressure system and the associated cold and warm fronts. We use the 291 K isentrope (empirically chosen) as a tracer of the location of the leading edge of the cold front. Additionally, forecasted atmospheric boundary mixing layer top heights from ERAI are used in the analysis of the vertical distribution of dust derived from AEROIASI.

3.4. Ground-Based Data Sets

As proxy for dust loads at the surface, we use horizontal visibility observations from a relatively dense network of meteorological stations over East Asia (from http://weather.uwyo.edu). Visibility observations are performed by automatic instruments, in some cases, and by observers looking at landmarks, in others. Visibility reports from human observers are naturally subjective to the individual observer, thus may not be quantitatively comparable from station to station. Low visibility can be caused by dust storms and also by fog, rain, and high anthropogenic pollution levels. In this study, we consider that the presence of dense dust plumes produces visibilities below 5 km, the presence of moderate dust loads produces visibilities between 5 and 8 km, and clean air exhibits visibility of at least 10 km.

Additional information on whether the dust layers are transported in the free troposphere or within the boundary layer is provided by ground-based lidars from the Japanese National Institute for Environmental Studies network [e.g., *Sugimoto et al.*, 2013]. Here we use time series of attenuated backscatter profiles from near the ground and up to 6 km of altitude (http://www-lidar.nies.go.jp), for tracing the vertical distribution of aerosols and clouds.

4. Dust Outbreak Over East Asia in Early March 2008

In this section, we describe the major dust storm over East Asia occurring from 1 to 3 March 2008, focusing on the 3D evolution of dust plumes observed by AEROIASI. This dust storm, originating from the Mongolian and North China deserts, spread largely over East Asia and prompted local authorities to warn populations about health risks, particularly those with respiratory disabilities (this dust event was reported on BCC News, http://news.bbc.co.uk/2/hi/asia-pacific/7274718.stm, and NASA's Earth Observatory, http://earthobservatory.nasa.gov/IOTD/view.php?id=8477).

In the following, we present the key phases of the dust outbreak, from the uplift phase starting on 29 February 2008 to the transport phase over the Sea on 3 March 2008. We shall do this by analyzing the daily evolution of the continuous 3D distribution of dusts over East Asia derived for the first time over both land and ocean from IASI using the AEROIASI method. This analysis focuses on the vertical pathways of dust and the role of vertical mixing in the convective boundary layer, which in some instances may mix dust down to the ground (thus affecting regional air quality). Moreover, we also illustrate the potential of AEROIASI to highlight the strengths and weaknesses of CHIMERE for simulating the 3D distribution of dust.

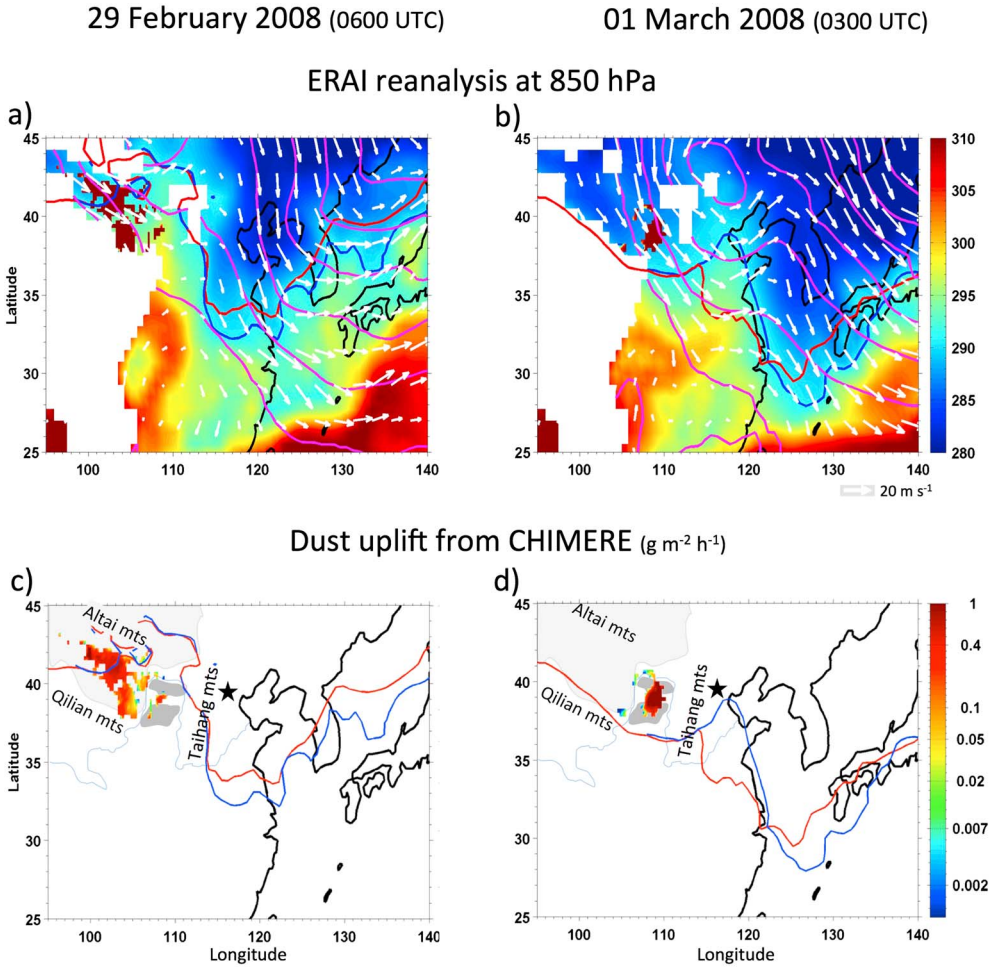

Figure 7. ERAI reanalysis at 850 hPa of equivalent potential temperatures (colors in K), winds (white arrows), and geopotential heights (pink contours for isolines every 40 m) over East Asia during the maxima of dust uplift (a) over the Gobi desert on 29 February 2008 at 0600 UTC and (b) in the vicinity of the Loess plateau on 1 March 2008 at 0300 UTC. (c and d) The corresponding CHIMERE-simulated dust emissions. Light and dark grey areas indicate the location of the dust sources respectively from the Gobi desert and the Loess plateau. The cold front edge associated to an extratropical cyclone is depicted by the 291 K isentrope at 850 hPa (blue contours) and at the surface (red contours). Figures 7c and 7d also show the location of the Yellow River (light blue line), the city of Beijing (black star), and the nearby mountains.

4.1. Dust Uplift From the Gobi Desert and the Loess Plateau

As is often the case for East Asian dust outbreaks, the dust storm in early March 2008 is triggered when an extratropical cyclone reaches the northern Asian dust source regions. On 29 February 2008, as the cyclone is forming, the associated low-pressure system is located on the western side of the Gobi desert (light grey-shaded areas in Figures 7c and 7d) and centered at 45°N 110°E (see pink isolines of geopotential height in Figure 7a). Although the cyclone structure is not clearly organized because of the orography, ERAI reanalyses show that strong surface winds (>12 m/s) are blowing in the warm sector of the cyclone (35–45°N 100–110°E) ahead of the cold front edge due to the cyclonic circulation around the low-pressure center and constriction between the Altai and Qilian mountains (see ERAI fields at 850 hPa in Figure 7a, whose level is located near the surface west of 112°E). The region over which the strong winds are blowing corresponds to the southeastern part of Gobi desert (Figures 7a and 7c) where intense dust emissions are simulated by CHIMERE between 0300 and 1200 UTC (Universal Time Coordinated; note that for China, UTC = LT − 8 h). Dust emissions occur over a relatively large area with a maximum around 0600 UTC (Figure 7c), mainly northwest of the Yellow River (light blue line in Figure 7c), and thus mainly associated with sandy and gravel soils, typical of the Gobi desert. Some dust is also lifted up in the vicinity of the Loess plateau (dust sources indicated as dark grey areas in Figures 7c and 7d).

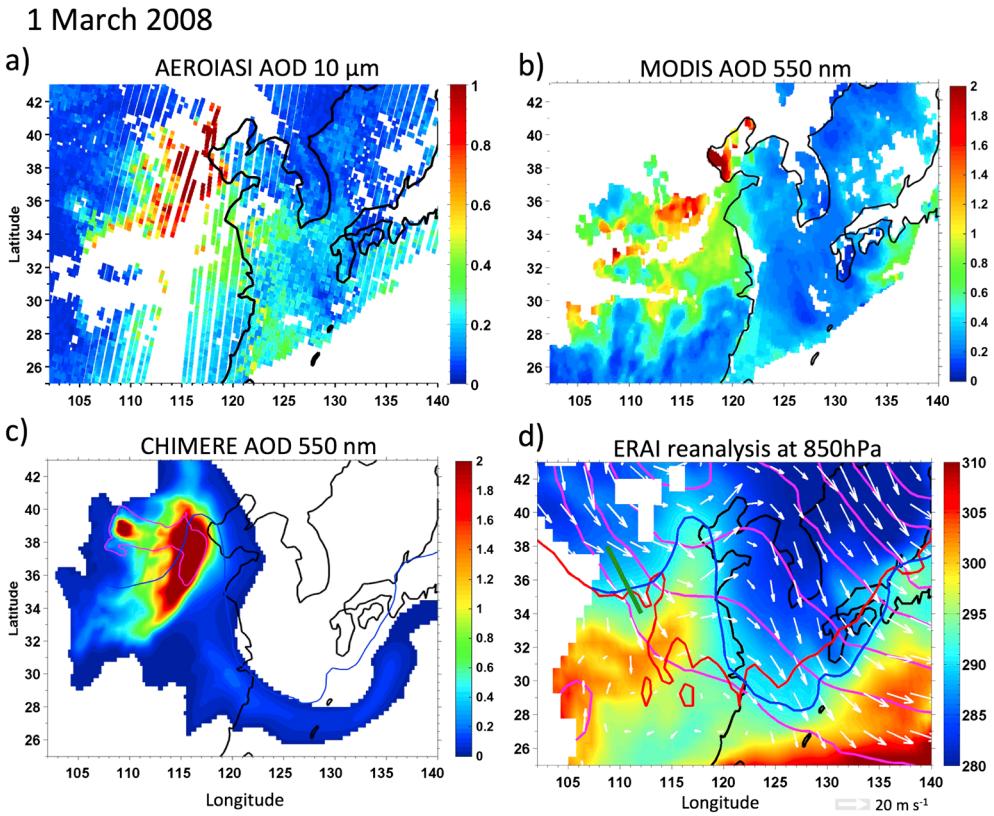

Figure 8. (a) AEROIASI observations of AOD at 10 μm over East Asia on 1 March 2008 at 0930 LT, (b) MODIS AOD at 550 nm derived with the Dark-Target approach for the same date and region at 1030 LT, (c) CHIMERE-simulated AOD at 550 nm at 0000 UTC and the location of dust emitted over the Loess plateau area (pink contours), and (d) ERAI reanalysis at 850 hPa at 0000 UTC of equivalent potential temperatures (colors in K), winds (white arrows), and geopotential heights (pink contours for isolines every 40 m). The cold front edge associated to an extratropical cyclone is depicted by the 291 K isentrope at 850 hPa (blue contours) and at the surface (red contours).

The following day (1 March), the extratropical cyclone moves southeastward (the low being centered at 42°N 117°E) with the well-defined cold (38–42°N 95–115°E) and warm (20–40°N 120–125°E) front edges forming the classical "lambda" shape. As the strong surface winds progress southeastward, a second intense dust uplift event occurs over the North Chinese deserts near the Loess plateau (dark grey in Figure 7d), on the southern side of the Yellow River. For this event, the uplift region is located behind the cold front edge (Figure 7b). According to CHIMERE, dust emissions last from 0000 to 0900 UTC on 1 March, and they are less spread horizontally than the previous day but with higher dust flux ($>1\,g\,m^{-2}\,h^{-1}$). Soils in this region are typically loess and sandy loess so that dusts emitted from these regions may have different optical properties than those emitted in the Gobi desert.

4.2. Dust Transport Over North China on 1 March 2008

During the morning (around 0000 UTC) of 1 March 2008, the extratropical cyclone is located north of the Beijing region (centered 43°N 115°E in Figure 8d) and the associated cold front already shows a well-defined edge (blue line west of 117°E in Figure 8d). At this time of the day, most dusts transported over North China correspond to that lifted the day before over the Gobi desert, while dust uplift close to the Loess plateau just begins (pink contours in Figure 8c, with some dust east of 112°E also emitted on 29 February).

4.2.1. Horizontal Distribution of Dust Plumes

At 0000 UTC, desert dusts uplifted over the Gobi desert are mainly distributed as a large rounded-shape plume (35–41°N 108–118°E) overpassing the Beijing region (see Figure 8c). This dense dust plume is consistently shown by the AOD horizontal distributions from AEROIASI (Figure 8a), CHIMERE (Figure 8c), and MODIS (south of 37°N; Figure 8b). We note that most of the dust from the Gobi desert is located ahead

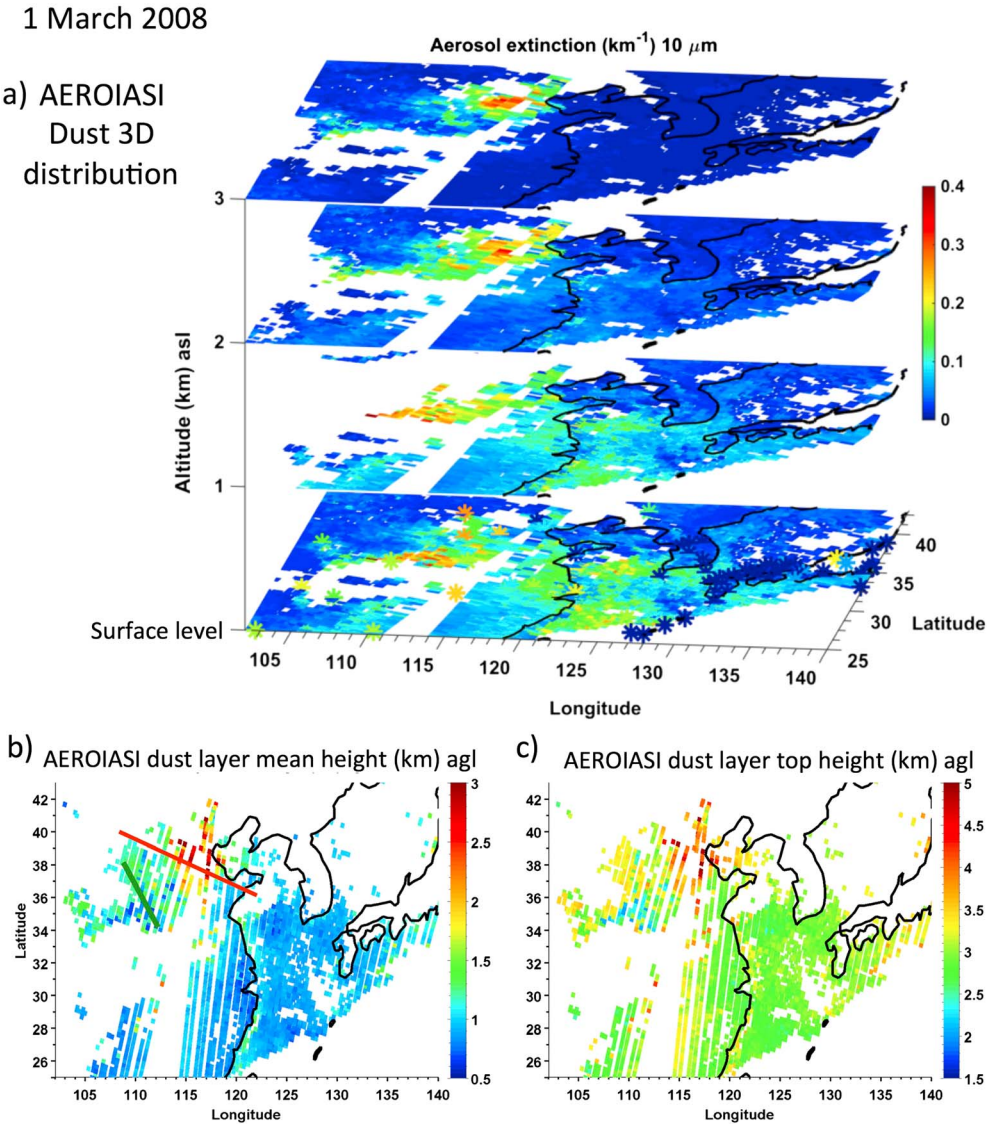

Figure 9. (a) 3D distribution of AEROIASI extinction coefficient for dust (km^{-1}) at 10 μm over East Asia on 1 March 2008 at 0930 LT, represented by slices at four altitudes: the surface level, 1, 2, and 3 km asl. Mean and top altitudes of dust layers derived from AEROIASI (for pixels with AODs at 10 μm above 0.2) are given in Figures 9b and 9c, respectively. Figure 9b shows the locations of the AEROIASI transects along the main dust plume (red straight line) and across the cold front (green straight line) in Figure 10. Horizontal visibility at the surface from numerous sites over East Asia is indicated in Figure 9a by *, where blue, green, orange, and red colors indicate respectively high (10 km), moderate (5 km), low (2 km), and very low (<1 km) visibilities.

of the cold front edge (blue line in Figure 8c), whereas the dust from the Loess plateau vicinity (39°N 110°E) is located behind the front (Figure 8c).

The AOD derived from AEROIASI, independently for each IASI pixel, shows a very good qualitative agreement with the structures depicted by MODIS, both for the main plume highlighted by AODs greater than 1 and other less dense dust plumes such as those observed over southeastern China and the East China Sea (e.g., south of 33°N and east of 115°E). AEROIASI retrieves the dust-related AOD over bright surfaces, such as the Gobi and northern China deserts (north of 37°N and west of 110°E in Figure 8a), where the MODIS observations derived in the visible with the Dark-Target are not available (Figure 8b). In this region, both AEROIASI and MODIS-DeepBlue (from the AQUA satellite, not shown) depict similar very low AOD north of 37°N and west of 109°E and two moderately dense dust plumes respectively located near 36°N/105°E and 39°N/110°E.

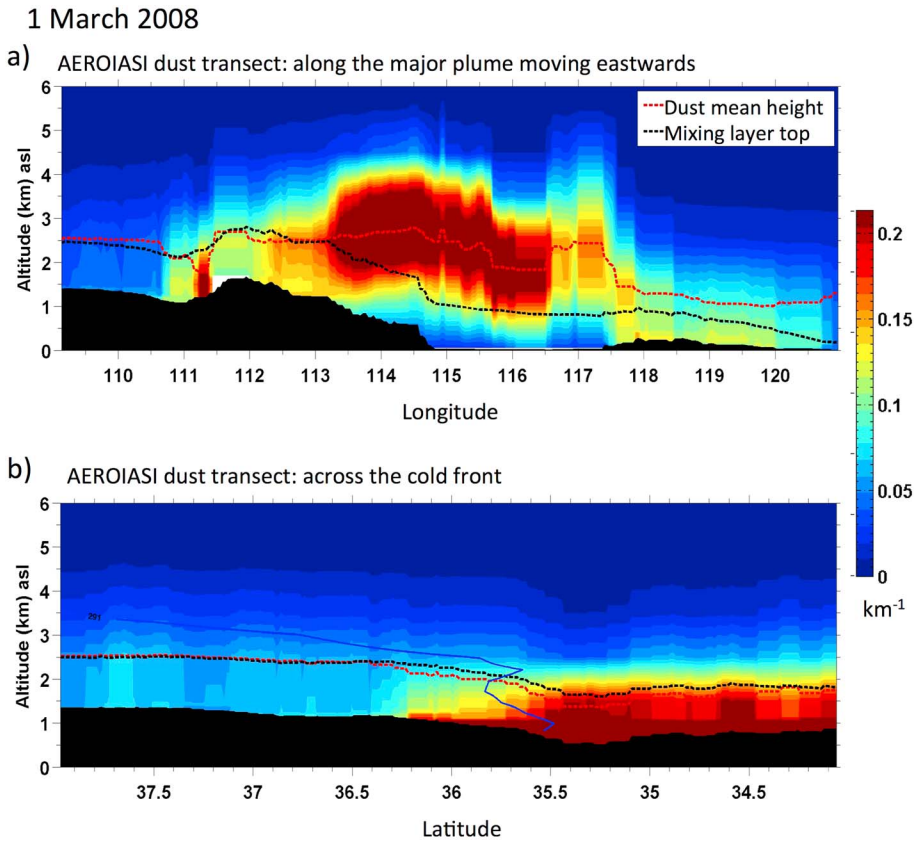

Figure 10. Transects of dust extinction coefficient profiles (km^{-1}) at 10 μm on 1 March 2008 at 0930 LT derived from AEROIASI: (a) along the major dust plume moving eastward and (b) across the cold front. Figure 9b (Figure 5d) also indicates the location of the AEROIASI transects (transect in Figure 10b).

4.2.2. 3D Distribution of Dust Layers

The 3D distribution of dust on 1 March is shown by a 3D map of aerosol extinction coefficient at 10 μm with horizontal slices for four different altitudes (Figures 9a) as well as mean and top heights of dust layers (Figures 9b and 9c) from AEROIASI. We clearly observe that the major dust plume (35–41°N 110–118°E) is separated from the ground, with a mean (top) altitude around 2.5 km agl (3.5 km agl) and reaching 3 km agl (4.5 km agl) at 39°N 115°E (Figures 9b and 9c). These regionally consistent features are derived by AEROIASI independently for cloud-free IASI pixel. For the area covered by this plume, the dust load near the surface derived by AEROIASI (Figure 9a at the surface level) is moderately high ($\alpha_{10\,\mu m}$ of ~0.15 km^{-1}) only west of 115°E and clearer air ($\alpha_{10\,\mu m}$ of ~0.05 km^{-1}) is remarked east of 115°E. This is consistent with the horizontal visibility estimations (* in Figure 9a at the surface level), which are moderate (<5 km) and high (~10 km) respectively west and east from 115°E. For higher altitudes (Figure 9a above 1 km asl), AEROIASI shows that dust extinction coefficients for the main dust plume are increasing up to ~2 km asl and decreasing above (3 km asl), where only the main dust plume is apparent.

Apart from the regions reached by the main dust plume, AEROIASI also shows structures of higher dust extinction coefficients near the surface (e.g., moderate dust plume reaching the east coast of China and over the East China Sea) only in the lower levels (in some cases reaching up to 1 km asl). These features of higher dust load at the surface are in good qualitative agreement with the horizontal visibility estimations (Figure 9a at the surface level). South of 37° over China and over the East China Sea, moderately high $\alpha_{10\,\mu m}$ (~0.15 km^{-1}) from AEROIASI are well correlated with moderate visibilities (e.g., over land at 30–32°N 120°E and over the Sea at 28°N 126°E). Over Japan and Korea, very low $\alpha_{10\,\mu m}$ (<0.05 km^{-1}) correspond to high horizontal visibilities (10 km).

Figure 10 shows two transects of dust vertical profiles from AEROIASI (see their locations in Figure 9b) selected so to analyze the 3D transport of the main dust plume (Figure 10a) and the location of dust with

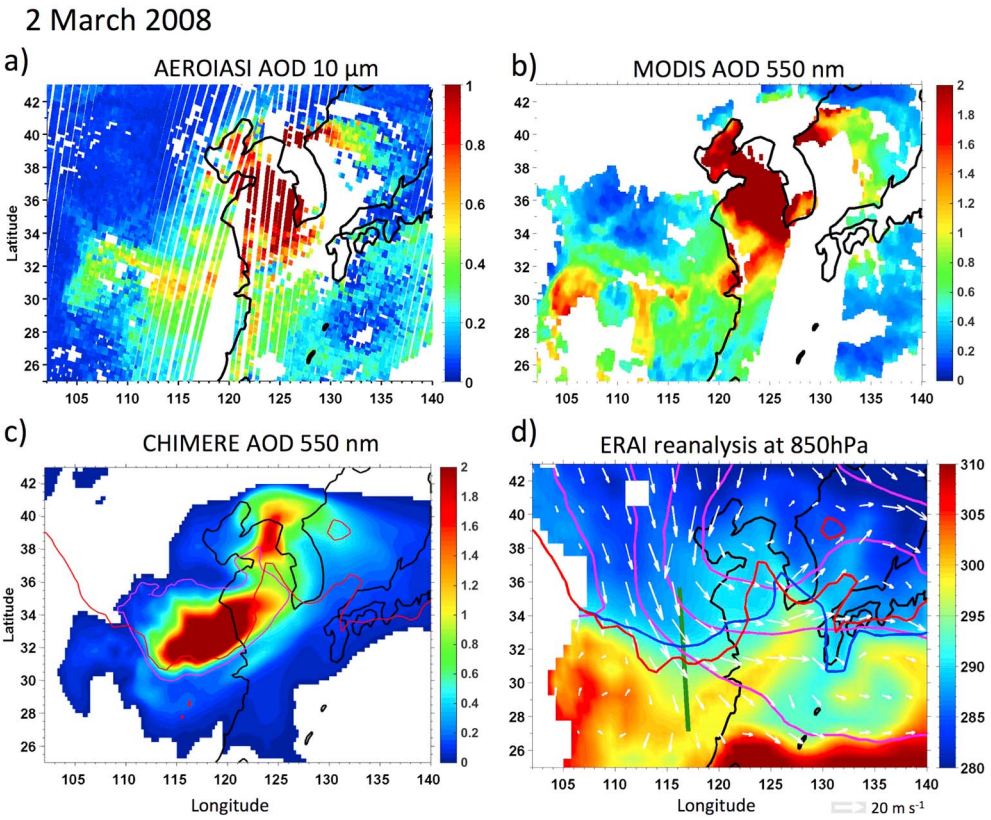

Figure 11. Same as Figure 8 but for 2 March 2008.

respect to the cold front progression (Figure 10b). The main dust plume (Figure 10a) is transported from west to east, coming from the elevated Loess plateau (west of 110°E), crossing over the Taihang Mountains (112°E, with ground level altitudes up to 1.8 km asl) with a mean altitude of ~2.5 km asl, until reaching the Beijing region (near 116°E). When leaving the mountainous regions east of 113°E, the dust plume is still transported at the same altitude, remaining around ~2.5 km asl, while being detached from the surface, because of the drop in terrain height. Indeed, the mixing atmospheric boundary layer top (black dashed line, estimated from ERAI reanalysis) does not seem to reach the dust layer east of 114°E, as it remains below ~1.2 km asl. During the previous evening, a shallow continental mixing layer might have allowed the detachment of the dust layer from the surface, presumably as a residual boundary layer.

While the core of the main dust plume is transported eastward, a part of the lifted dust is also transported in the southeastward direction following the strong winds perpendicular to the cold front edge (see blue and green lines around 36°N 110°E in Figure 8d). In the transect of Figure 10b, we clearly observe that at this moment, desert dusts following this pathway are located behind the cold front edge (blue line) and they are transported within a 1 km deep mixing boundary layer. The cold front edge (north of 35.5°N) from the surface and up to ~3 km asl is located ahead of the dust plume, and both move southeastward at high speeds (~20 m s^{-1}).

4.3. Dust Over Central China and the Yellow Sea on 2 March 2008

In the morning of 2 March, the cyclone arrives to the Korean peninsula and the low-pressure system is centered at 40°N/125°E after traveling over ~1200 km in the previous 24 h (Figure 11d). Desert dusts emitted from both the Gobi desert and the Loess plateau vicinity are massively spreading over the continent.

4.3.1. Horizontal Distribution of Dust Plumes

AEROIASI (Figure 11a) and MODIS (Figure 11b) consistently show widespread and dense dust plumes covering a very large area from 30°N/105°E to 40°N/135°E, with the highest AODs over the Yellow Sea. Dust plumes roughly form an "S," with the northeastern part of the plume reaching the center of the cyclone. CHIMERE simulates a similar overall distribution of dust and allows identifying the source regions of the dust plumes (Figure 11c). CHIMERE suggests that the dust plume freshly uplifted 21 h before near the

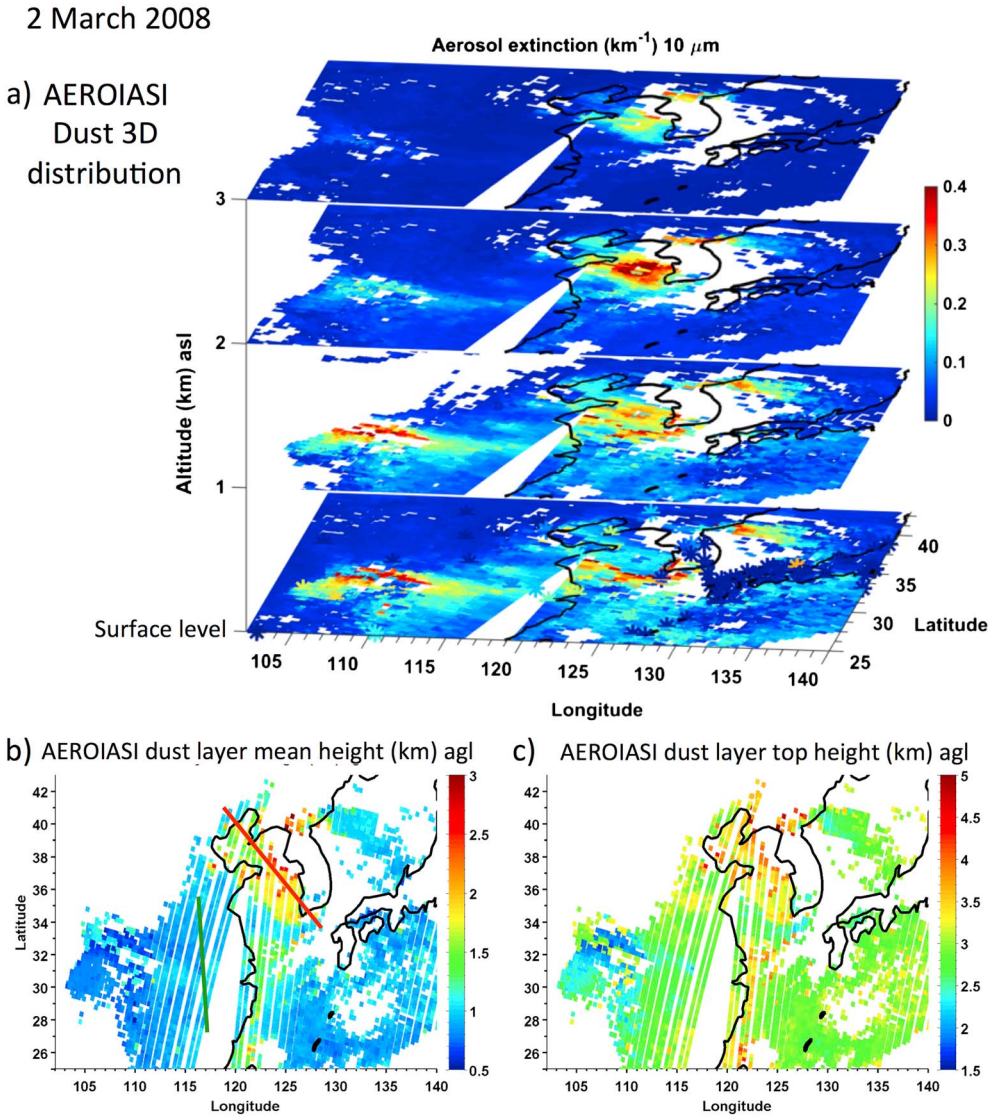

Figure 12. Same as Figure 9 but for 2 March 2008.

Loess plateau spreads over central-east China and part of the Yellow Sea (pink contours in 31–37°N 110–125°E in Figure 11c). Around this plume, desert dusts from the Gobi desert form a larger dust envelope, spreading further south, southeast, and northeast (see dust from the Gobi desert outside the pink contours in Figure 11c). The structure of the observed plumes is well simulated with CHIMERE, although CHIMERE AODs seem to be overestimated for dusts emanating from the Loess plateau and underestimated for that emanating from the Gobi desert, with respect to satellite observations.

Dust plumes over central-east China move along with the cold front edge, which shows a more complex vertical structure than the previous day (see cold front edge at the surface in red and at 850 hPa in blue in Figures 11c and 11d). Over the continent, the cold front moves southeastward faster at the surface than at 850 hPa. There, the front edge at the surface clearly delimits the dust plume emitted near the Loess plateau (31°N 112–120°E, Figure 11c), while it is slightly behind at higher altitudes (850 hPa in Figure 11d). Over the ocean (33–37°N 122°E), cold air masses progress eastward but slower at the surface than at 850 hPa. At the surface, the cold front progression seems to slow down when encountering warmer oceanic air masses and only above, at 850 hPa, is the cold front edge collocated with the dust front from the Loess plateau (Figure 11c). Southeast of the Yellow Sea (33–37°N 125–127°E), dust ahead of the cold front edge likely comes from the first uplift event at Gobi desert.

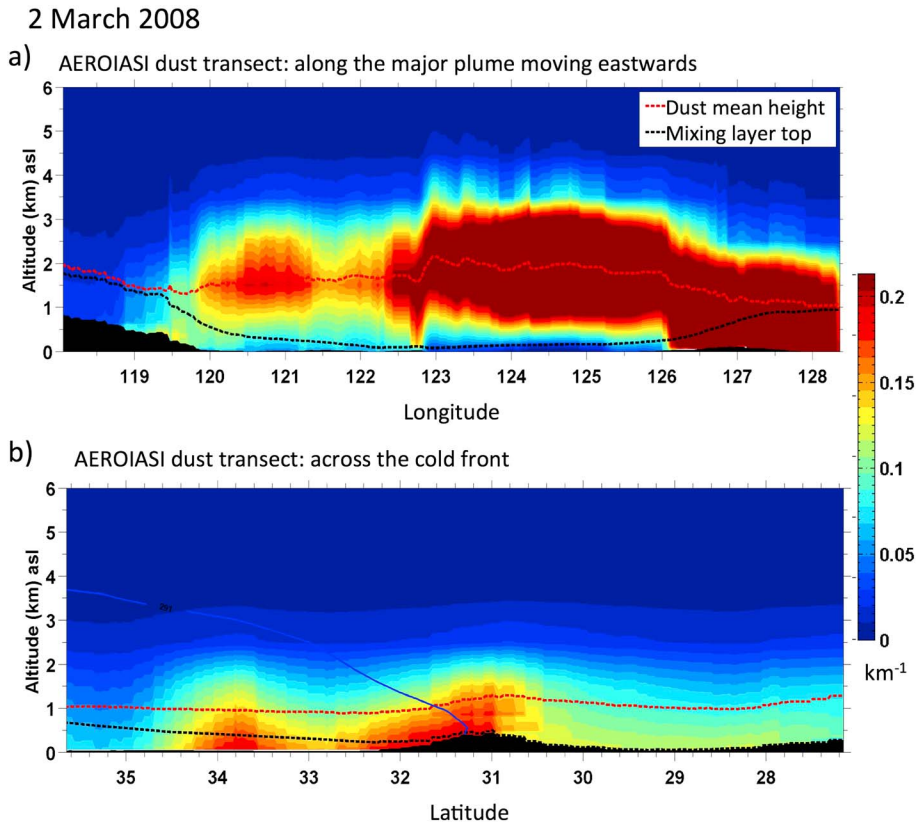

Figure 13. Same as Figure 10 but for 2 March 2008.

4.3.2. 3D Distribution of Dust Layers

According to AEROIASI observations on 2 March (Figure 12), the densest dust plume overpasses the Yellow Sea (34–40°N 120–126°E) at an elevated mean altitude of ~2.5 to ~3 km (Figure 12b), with its top reaching ~3.5 to ~4 km agl (Figure 12c). Most of the dust layer consistently remains at similar mean altitudes as the previous day (when the dust layer was mostly located over the continent). North of ~35°N, the dust plume is elevated and detached from the ground. The altitude of the elevated dust layer gradually increases toward the north until reaching the highest altitude approaching the center of the low-pressure system (Figure 12a). This is likely linked to the ascending motions (~180 m/h according to ERAI) near the core of the extratropical cyclone (40°N 125°E). South of the Yellow Sea (32–34°N 120–126°E), the plume reaches the ground. This slantwise distribution of dust ascending from south to north (from 32 to 39°N) is clearly consistent with that derived from the CALIOP lidar transect at 1730 UTC over the Yellow Sea (Figure 4a) and also AEROIASI observations at 1230 UTC (Figure 4b). Moreover, CHIMERE simulations of the dust extinction profiles (Figure 4d) show a fair overall agreement with those observed with AEROIASI and CALIOP, as they all depict a low-level dust layer over the Yellow Sea (from 33°N to 37°N) which rises northward up to a mean altitude around 3 km asl and also a dense low-level plume which is located south of the Yellow Sea (near 29°N). Small differences in the horizontal location of these dust plumes (1 to 2 degrees) are noted between the model and the observations. However, almost no dust is simulated between 31°N to 33°N in discrepancy with observations, and the simulated low-level dust layer (from 33°N to 37°N) is much less dense as compared to CALIOP, AEROIASI, and MODIS retrievals (respectively Figures 4a, 4b, and 11b).

Further information on the link between the vertical distributions of dust plumes and the atmospheric thermodynamical structure is given in Figure 13. We clearly notice that the major elevated dust plume over the Yellow Sea (120–126°E in Figure 13a) is transported over a very shallow marine boundary layer (below 300 m agl), whose top does not reach the dust layer. However, the dust plume is mixed down to the surface when encountering a deeper marine mixing boundary layer (up to 1 km agl) east of 126°E.

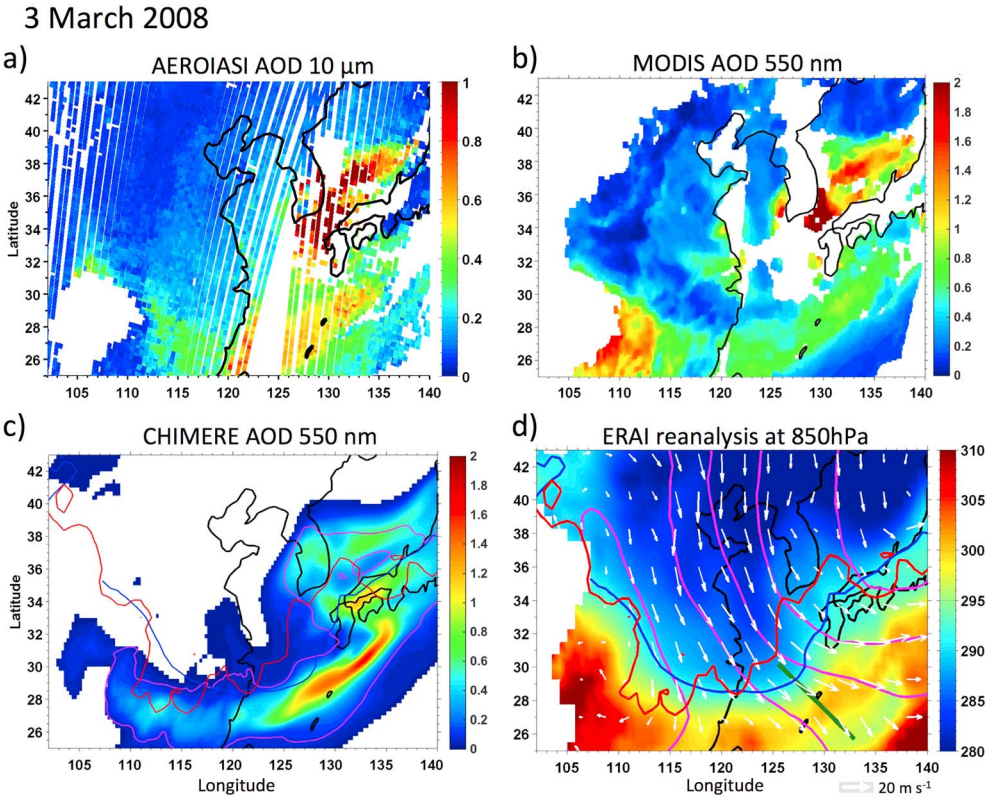

Figure 14. Same as Figure 8 but for 3 March 2008.

Indeed, the dust plume is entrained into the mixed layer as the marine layer deepens over the warmer sea surface temperatures.

Dust plumes over continental China are mostly located near the surface and extending up to ~1.5 to ~2.5 km (respectively west and east of 110°E; Figure 12a), as observed the previous day. These dust plumes follow the southeastward progression of the cold front and remain within the lowest part of the troposphere (Figure 13b). Dust plumes originating from the Loess plateau are located behind the cold front edge (between 33°N and 35°N). Other dust plumes are observed at the edge or ahead of the front (30–33°N). Moreover, the horizontal distribution of these continental dust plumes is in good agreement with the moderate visibilities reported at the SYNOP stations (Figure 12a at the surface level), as well as high visibilities for the regions with very low dust loads ahead of the dust plumes (north of 34°N and west of 115°E) and over Japan.

4.4. Dust Reaching the Japan Sea and the Pacific on 3 March 2008

On 3 March, the extratropical cyclone progresses further east up to northern Japan, with a less marked low located east of 140°E (outside the region of analysis; Figure 14d). The cyclonic circulation loses intensity, the temperature gradient associated to the cold front is less marked, and the "lambda" shape between the cold and warm fronts is no longer apparent.

4.4.1. Horizontal Distribution of Dust Plumes

Two major dust plumes are observed by AEROIASI, in consistency with MODIS (Figures 14a and 14b). The denser dust plume, observed over the Yellow Sea the previous day, reaches the Japan Sea on 3 March (32–39°N 127–140°E; Figures 14a and 14b). Desert dusts coming from central-east China, uplifted over the Gobi desert and near the Loess plateau, form a separate elongated plume from southern China (28°N/110°E) to the East China Sea south of Japan (34°N/125°E). CHIMERE simulates these dust plumes (Figure 14c) and suggests that they are composed of dust from both the Loess plateau area (pink counters) and the Gobi desert. MODIS also observes high AOD over southern China (20–30°N 105–115°E), which is likely associated to aerosols from wildfires, as suggested by MODIS fire detections (http://rapidfire.sci.gsfc.nasa.gov).

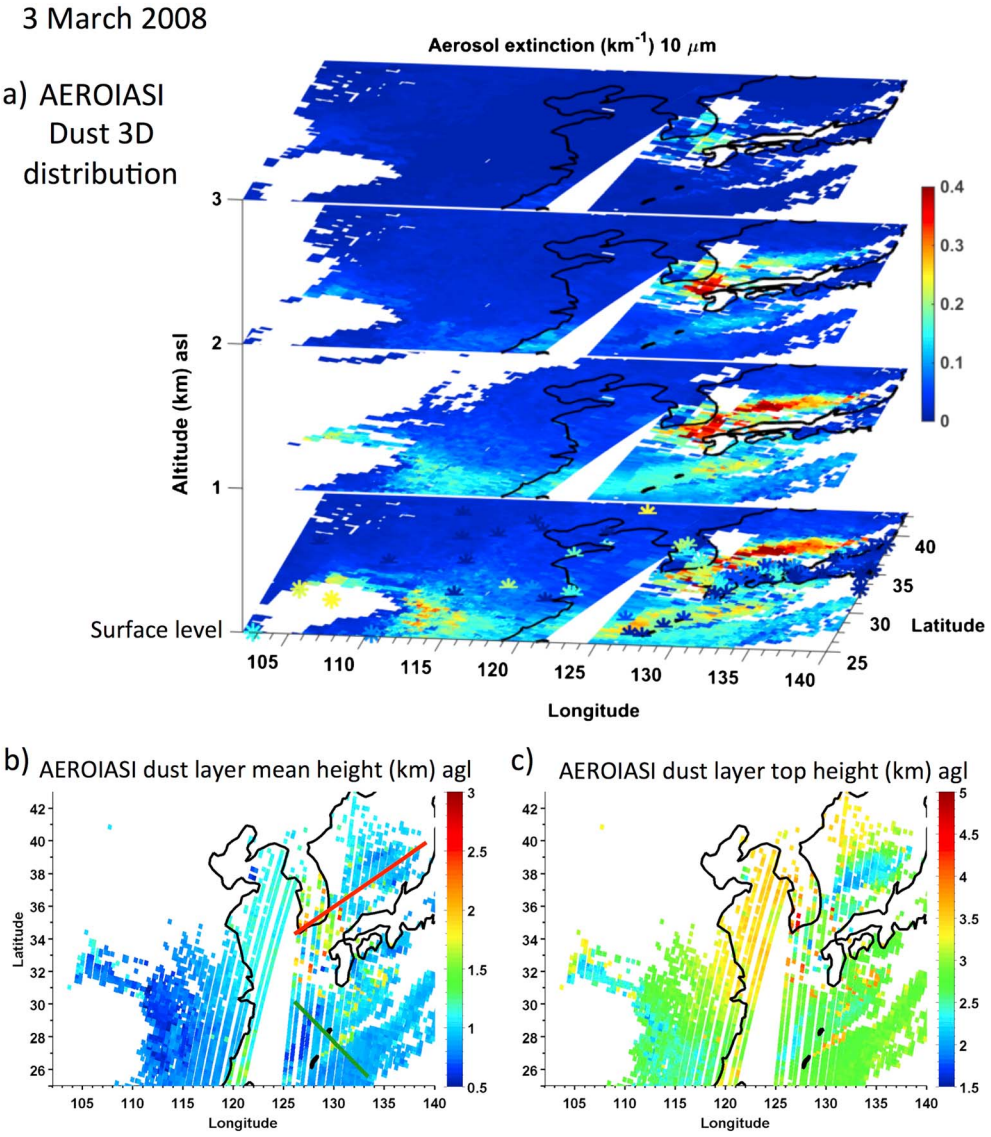

Figure 15. Same as Figure 9 but for 3 March 2008.

Figure 14c shows that the whole dust plume south of Japan is transported ahead of the cold front edge, indicated by the 291 K isentrope. As noted the previous day over the East China Sea, this edge moves faster in altitude (at 850 hPa) than at the surface. Warmer oceanic air masses near the surface likely mix with the cold front, slowing it down and therefore allowing for the elevated dust layers to move ahead of the surface front.

4.4.2. 3D Distribution of Dust Layers

AEROIASI shows that the northern dust plume is elevated only between the South Korean and Japanese coasts (35°N 130°E; Figure 15a at 2 km asl), with a mean altitude of ~1.5 km agl (and layer top altitude of ~3 km agl). Further northeast, this dust layer descends until reaching the surface over the Japan Sea (north of 37°N and east of 130°E; Figure 15a), with the mean and top altitudes of the layer being ~1 km agl and ~2.2 km agl, respectively (Figures 15b and 15c). An AEROIASI vertical transect across this dust plume (Figure 16a) provides evidence that dust is mixed down to the surface at the locations where the marine boundary layer is deeper (up to 1.5 km over the Japan Sea, north of 130°N), but remains separated from the surface where the mixing boundary layer is shallower than over the Japan Sea and its top does not reach the lower part of the dust layer (128.5–129°E in

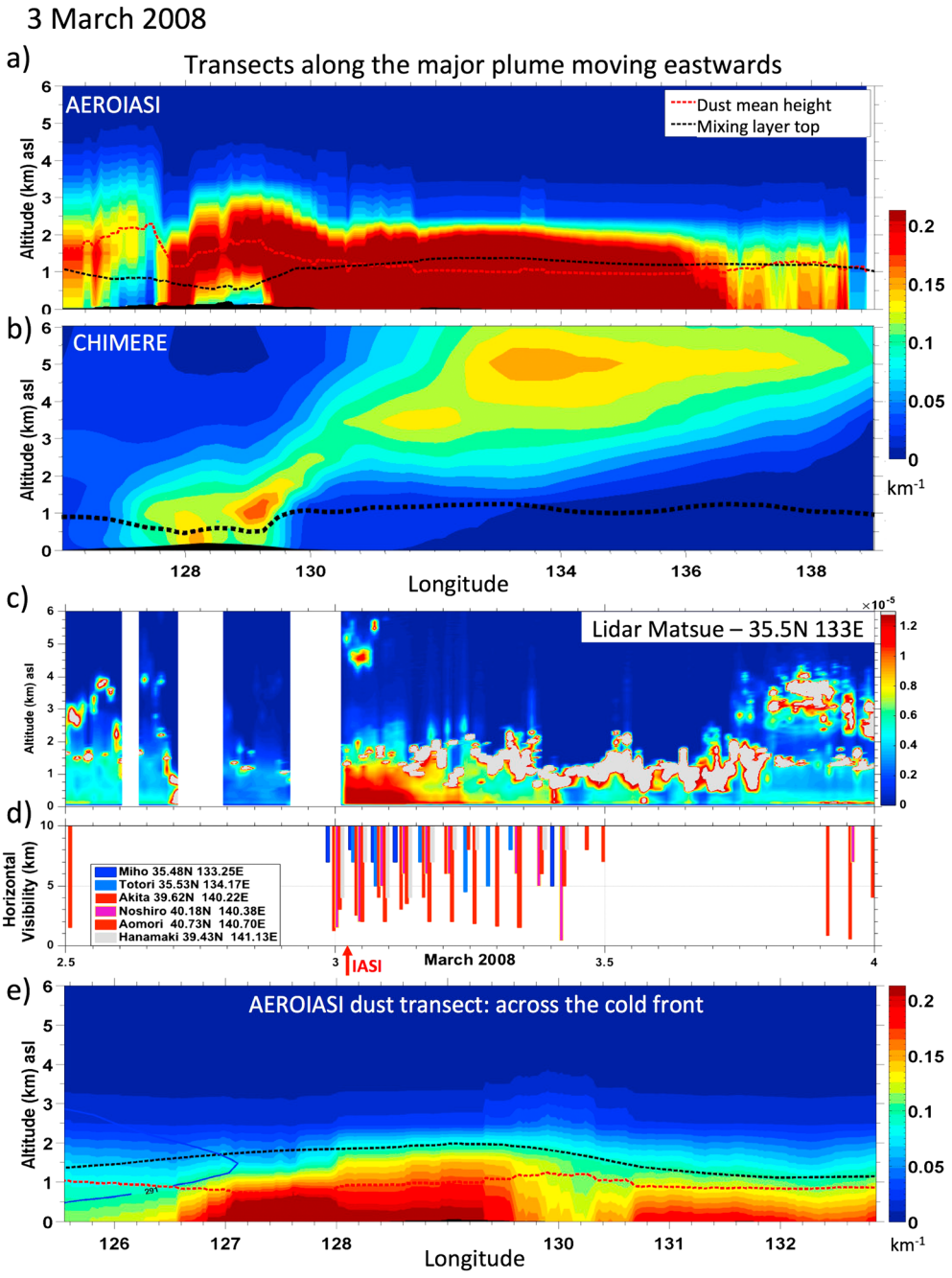

Figure 16. Major dust plume moving eastward on 3 March 2008: transects of dust extinction coefficient profiles derived from (a) AEROIASI (10 μm) at 0930 LT and (b) CHIMERE (550 nm) at 0800 LT (0000 UTC), (c) time series of vertical profiles of attenuated backscatter coefficients measured by a ground-based lidar at Matsue (35.5°N 133°E) on 2 and 3 March 2008 (clouds are indicated in grey), and (d) horizontal visibility at the surface from six sites over Japan on 2 and 3 March 2008 (a red arrow indicates the IASI overpass time). (d) AEROIASI dust transect across the cold front, as Figure 10b but for 3 March 2008.

Figure 16a). The deeper growth of the marine boundary layer over the Japan Sea is associated with large temperature gradients between the sea surface and the overlaying air (ERAI reanalyses show skin temperatures 4 to 6°C higher than at 2 m asl). This positive surface temperature anomaly over the Japan Sea with respect to the surrounding areas is confirmed by NOAA satellite observations (http://www.esrl.noaa.gov/psd).

Ground-based observations (Figures 16c and 16d) clearly confirm that these dust layers transported over the Japan Sea and arriving on the western Japanese coast do reach the surface. The time series of lidar profiles measured at Matsue (35.5°N 133°E; Figure 16c) clearly depicts an increase of near surface aerosol load (in red colors) in the morning of 3 March, much likely associated to the arrival of dust. These observations show aerosol layers mainly extending from the surface and up to ~2.2 km agl (in good agreement with AEROIASI), with some significantly thinner layers around ~5 km agl. The increase of dust load near the surface is also shown by the concomitant reduction of horizontal visibility (to values less than 5 km) in the morning of 3 March, near Matsue and also in northern Japan (respectively in blue and red in Figure 16d). On the other hand, the dust layer simulated by CHIMERE over the Japan Sea is located in the free troposphere, extending from 2 to 6 km asl, and is not entrained into the boundary layer and mixed down to the surface (Figure 16b). This discrepancy with observations is likely associated with the fact that the simulated dust layer is transported too high in the troposphere and that the lower part of the dust plume is not reached by the top of the convective boundary layer simulated with CHIMERE (black dashed line in Figure 16b).

The other major dust layer, located south of Japan, is transported over the Pacific Ocean (south of 31°N) extending from the ground and up to 1 to 2.5 km agl (Figures 15a and 15c), similarly to what was observed over the continent the previous day. As previously mentioned, this dust plume is transported ahead of the cold front and its nose peaks at 1.5 km agl (see transect of Figure 16e). Just ahead of the cold front, a deeper dust layer is observed (128–129.5°E) and a thinner one further away from the front (131–133°E). Both dust layers are located within the marine mixing layer (estimated by ERAI reanalyses). The top of the marine boundary layer derived from ERAI reanalyses is in remarkable agreement with the dust layer top depicted by AEROIASI.

5. Discussion

We have analyzed the 3D evolution of a major dust outbreak over East Asia in early March 2008 using new aerosol retrievals derived from IASI satellite observations. To the authors' knowledge, this is the first analysis showing the daily evolution of the continuous 3D distribution of desert dust plumes using satellite observations both over land and ocean, with an unprecedented coverage of 95% of IASI cloud-free pixels. This has been achieved through the development of the innovative approach called AEROIASI based on online radiative transfer calculations and an auto-adaptive Tikhonov-Phillips regularization. It was conceived as a flexible tool, able to produce quality-assured aerosol retrievals in large variety of atmospheric conditions and surface characteristics.

The AEROIASI method allows deriving vertical profiles of dust extinction coefficients at 10 μm for individual cloud-free IASI pixels, both over land and ocean. The vertical distribution of dust layers described by AEROIASI agrees remarkably well with that observed along CALIOP transects acquired during the case study. AEROIASI enables the observation of dust layers, both elevated ones and those reaching the surface, in terms of mean and top altitudes with low mean biases ($<$110 m), high linear correlations (0.95 and 0.91, respectively, for mean and top altitudes), and good mean precisions (260 m and 350 m, respectively) with respect to CALIOP.

Furthermore, the dust AOD retrievals using AEROIASI are in good agreement with the coarse mode AOD derived from 13 AERONET stations over East Asia. Comparisons from 7 months of measurements in 2008 show very low mean bias ($<$1%), a mean precision of ~0.1 (RMS differences), and linear correlation coefficients of ~0.8. Regional biases are noted, particularly far away from the dust source regions, i.e., east of 125°E.

The horizontal distribution of dust plumes observed by AEROIASI and MODIS during the 1–3 March case study is found to be very similar. Dust plumes depicted by MODIS are slightly shifted eastward, consistent with the fact that the MODIS overpass is 1 h after that of IASI and that the flow is westerly. It is worth noting that there is consistency in the AEROIASI AOD fields derived across marked surface transitions such as desert regions and neighboring continental regions (e.g., north and south of 37°N, respectively) as well as between land and the nearby sea (e.g., at 37°N 117°E or 34°N 120°E). In the latter case, AEROIASI AOD fields are found to be more homogenous than their MODIS counterparts, which rely on different algorithms over land and sea. Quantitative differences in AOD between AEROIASI and MODIS may be attributed to the difference in wavelength; as for dust plumes in Figure 8, the AOD at 10 μm is a factor ~2 weaker than that at 500 nm, consistent with the typical spectral dependence of the AOD for desert dust (corresponding to Angström exponents between 10 μm and 500 nm of ~0.2 to ~0.4). Other differences may also come from the fact that MODIS retrievals also depict fine mode particles (dust or other type of aerosols).

6. Conclusions

The major dust outbreak over East Asia described by AEROIASI originates from strong surface winds associated to an extratropical cyclone crossing over the Mongolian and North Chinese deserts. Ahead of the cold fronts associated with the cyclone, a first major dust plume is lifted over the Gobi desert. The following day, AEROIASI shows how dust travels over the Mongolian plateau and the Taihang Mountains, and then overpasses the Beijing region at the same altitude as over the mountains. Behind the cold front edge, a second major dust front is emitted near the Loess plateau. The next day, both dust plumes form a very large dust belt extending from southeast to northeast across most East Asia, with the highest AOD values over the Yellow Sea. According to AEROIASI, this dense dust layer is mixed down to the sea surface only over the southern Yellow Sea, where warm sea surface temperatures enable the development of a deep marine mixing layer entraining into the dust layer. Over the northern Yellow Sea, the dust layer remains elevated at ~2.5 km (mean altitude) over shallower marine boundary layers due to cooler sea surface temperatures than further south. This dust layer is lifted even higher while approaching the low-pressure system core, likely due to the associated ascending motions. On the last day of the analyzed case study, the major dust plume, previously transported as elevated layers over the northern Yellow Sea, encounters a deep mixing boundary layer over the Japan Sea, which mixes it down to the surface, as also observed with ground-based lidar and SYNOP station observations acquired over Japan. CHIMERE reproduces the slantwise vertical distribution of dust rising northward over the Yellow Sea, but it simulates a dust layer located too high in the free troposphere over the Japan Sea. This comparison illustrates the potential of AEROIASI retrievals for evaluating the 3D distribution of dust modeled by CHIMERE.

This study has shown the great potential of AEROIASI to analyze the 3D distribution of desert dust, the link with atmospheric dynamics, and its impacts on the environment (which may be closely related to its 3D distribution). Future analysis will also focus on the 3D distribution and dynamics of dust from the greatest sources on Earth, i.e., the Sahara desert. The use of regional desert dust properties [as those from, e.g., *Di Biagio et al.*, 2014b], as well as additional spectral bands for joint retrievals of the particle size or meteorological variables relevant for the dust retrieval (e.g., atmospheric temperature profiles), will be considered.

Acknowledgments

The authors are grateful for the financial support given by the Centre National des Etudes Spatiales (CNES, the French Space Agency), the Université Paris Est Créteil (UPEC), the Centre National des Recherches Scientifiques – Institut National des Sciences de l'Univers (CNRS-INSU), and the Programme National de Télédétection Spatiale (PNTS, http://www.insu.cnrs.fr/actions-sur-projets/pnts-programme-national-de-teledetection-spatiale, grant PNTS-2013-05, project "SYNAEROZON") for achieving this research work and its publication. This study also was financed by the project "IASI-TOSCA" (Terre, Océan, Surfaces continentals, Atmosphère) from CNES and by a "Chaire d'Excellence" of UPEC and CNES. IASI is a joint mission of EUMETSAT and CNES. We acknowledge the support by the data centers ETHER (http://www.pole-ether.fr), ICARE (http://www.icare.univ-lille1.fr), and NASA (http://ladsweb.nascom.nasa.gov) for providing respectively data sets from IASI (level 1C, originally supplied by EUMETSAT through the Eumetcast system distribution, http://www.eumetsat.int), CALIPSO (level 1), and MODIS (level 2). Meteorological reanalyses are produced by ECMWF and supplied by CLIMSERV (http://climserv.ipsl.polytechnique.fr). We acknowledge the University of Wyoming (Larry Oolman) for providing the horizontal visibility data sets (http://weather.uwyo.edu), the National Institute for Environmental Studies for ground-based lidar measurements (http://www-lidar.nies.go.jp), the AERONET network for sun photometer observations over East Asia (http://aeronet.gsfc.nasa.gov), and the NOAA/OAR/ESRL PSD (Boulder, Colorado, USA; http://www.esrl.noaa.gov/psd) for the NOAA_OI_SST_V2 data. We thank G. Foret, C. Di Biagio, and P. Formenti from LISA for fruitful discussions on desert dust.

References

Ackerman, S. A. (1997), Remote sensing aerosol using satellite infrared observations, *J. Geophys. Res.*, *102*(D14), 17,069–17,079, doi:10.1029/96JD03066.

Alfaro, S. C., and L. Gomes (2001), Modeling mineral aerosol production by wind erosion: Emission intensities and aerosol size distributions in source areas, *J. Geophys. Res.*, *106*(D16), 18,075–18,084, doi:10.1029/2000JD900339.

Banks, J. R., H. E. Brindley, C. Flamant, M. J. Garay, N. C. Hsu, O. V. Kalashnikova, L. Klüser, and A. M. Sayer (2013), Intercomparison of satellite dust retrieval products over the west African Sahara during the Fennec campaign in June 2011, *Remote Sens. Environ.*, *136*, 99–116.

Brindley, H., P. Knippertz, C. Ryder, and I. Ashpole (2012), A critical evaluation of the ability of the Spinning Enhanced Visible and Infrared Imager (SEVIRI) thermal infrared red-green-blue rendering to identify dust events: Theoretical analysis, *J. Geophys. Res.*, *117*, D07201, doi:10.1029/2011JD017326

Capelle, V., A. Chédin, M. Siméon, C. Tsamalis, C. Pierangelo, M. Pondrom, R. Armante, C. Crevoisier, L. Crépeau, and N. A. Scott (2014), Evaluation of IASI derived dust aerosols characteristics over the tropical belt, *Atmos. Chem. Phys.*, *14*, 9343–9362.

Carrer, D., J.-L. Roujean, O. Hautecoeur, and T. Elias (2010), Daily estimates of aerosol optical thickness over land surface based on a directional and temporal analysis of SEVIRI MSG visible observations, *J. Geophys. Res.*, *115*, D10208, doi:10.1029/2009JD012272.

Cattrall, C., J. Reagan, K. Thome, and O. Dubovik (2005), Variability of aerosol and spectral lidar and backscatter and extinction ratios of key aerosol types derived from selected Aerosol Robotic Network locations, *J. Geophys. Res.*, *110*, D10S11, doi:10.1029/2004JD005124.

Chiapello, I., C. Moulin, and J. M. Prospero (2005), Understanding the long-term variability of African dust transport across the Atlantic as recorded in both Barbados surface concentrations and large-scale Total Ozone Mapping Spectrometer (TOMS) optical thickness, *J. Geophys. Res.*, *110*, D18S10, doi:10.1029/2004JD005132.

Clarisse, L., D. Hurtmans, A. J. Prata, F. Karagulian, C. Clerbaux, M. De Mazière, and P.-F. Coheur (2010), Retrieving radius, concentration, optical depth, and mass of different types of aerosols from high-resolution infrared nadir spectra, *Appl. Optic.*, *49*(19), 3713–3722.

Clarisse, L., P.-F. Coheur, F. Prata, J. Hadji-Lazaro, D. Hurtmans, and C. Clerbaux (2013), A unified approach to infrared aerosol remote sensing and type specification, *Atmos. Chem. Phys.*, *13*, 2195–2221, doi:10.5194/acp-13-2195-2013.

Clarke, A. D., et al. (2004), Size distributions and mixtures of dust and black carbon aerosol in Asian outflow: Physiochemistry and optical properties, *J. Geophys. Res.*, *109*, D15S09, doi:10.1029/2003JD004378.

Clerbaux, C., et al. (2009), Monitoring of atmospheric composition using the thermal infrared IASI/MetOp sounder, *Atmos. Chem. Phys.*, *9*(16), 6041–6054.

Cuesta, J., J. Marsham, D. Parker, and C. Flamant (2009), Dynamical mechanisms controlling the vertical redistribution of dust and the thermodynamic structure of the West Saharan Atmospheric Boundary Layer during Summer, *Atmos. Sci. Lett.*, doi:10.1002/asl.207.

Cuesta, J., et al. (2013), Satellite observation of lowermost tropospheric ozone by multispectral synergism of IASI thermal infrared and GOME-2 ultraviolet measurements over Europe, *Atmos. Chem. Phys.*, *13*(19), 9675–9693.

d'Almeida, G. A. (1987), On the variability of desert aerosol radiative characteristics, *J. Geophys. Res.*, *92*(D3), 3017–3026, doi:10.1029/JD092iD03p03017.

Dee, D., et al. (2011), The ERA-Interim reanalysis: Configuration and performance of the data assimilation system, *Q. J. R. Meteorol. Soc.*, *137*, 553–597, doi:10.1002/qj.828.

Deirmendjian, D., R. Clasen, and W. Viezee (1961), Mie scattering with complex index of refraction, *J. Opt. Soc. Am.*, *51*(6), 620–633, doi:10.1364/JOSA.51.000620.

DeSouza-Machado, S. G., et al. (2010), Infrared retrievals of dust using AIRS: Comparisons of optical depths and heights derived for a North African dust storm to other collocated EOS A-Train and surface observations, *J. Geophys. Res.*, *115*, D15201, doi:10.1029/2009JD012842.

Di Biagio, C., P. Formenti, S. A. Styler, E. Pangui, and J.-F. Doussin (2014a), Laboratory chamber measurements of the longwave extinction spectra and complex refractive indices of African and Asian mineral dusts, *Geophys. Res. Lett.*, *41*, 6289–6297, doi:10.1002/2014GL060213.

Di Biagio, C., H. Boucher, S. Caquineau, S. Chevaillier, J. Cuesta, and P. Formenti (2014b), Variability of the infrared complex refractive index of African mineral dust: Experimental estimation and implications for radiative transfer and satellite remote sensing, *Atmos. Chem. Phys.*, *14*, 11,093–11,116.

Diner, D. J., et al. (2001), MISR level 2 aerosol retrieval algorithm theoretical basis, rev. E, JPL-D11400, Jet Propul. Lab., Pasadena, Calif.

Dubovik, O., B. N. Holben, T. Lapyonok, A. Sinyuk, M. I. Mishchenko, P. Yang and I. Slutsker (2002), Non-spherical aerosol retrieval method employing light scattering by spheroids, *Geophys. Res. Lett.*, *29*(10), 1415, doi:10.1029/2001GL014506.

Dunion, J. P., and C. S. Velden (2004), The impact of the Saharan air layer on Atlantic tropical cyclone activity, *Bull. Am. Meteorol. Soc.*, *85*(3), 353–365.

Fernald, F. G. (1984), Analysis of atmospheric lidar observations—Some comments, *Appl. Optic.*, *23*(5), 652–653.

Fernald, F. G., B. M. Herman and J. A. Reagan (1972), Determination of aerosol height distributions by lidar, *J. Appl. Meteorol.*, *11*, 482–489,.

Foret, G., G. Bergametti, F. Dulac, and L. Menut (2006), An optimized particle size bin scheme for modeling mineral dust aerosol, *J. Geophys. Res.*, *111*, D17310, doi:10.1029/2005JD006797.

Haywood, J., and O. Boucher (2000), Estimates of the direct and indirect radiative forcing due to tropospheric aerosols: A review, *Rev. Geophys.*, *38*(4), 513–543, doi:10.1029/1999RG000078.

Hess, M., P. Koepke, and I. Schult (1998), Optical properties of aerosols and clouds: The software package OPAC, *Bull. Am. Meteorol. Soc.*, *79*(5), 831–844.

Holben, B. N., et al. (1998), AERONET—A federated instrument network and data archive for aerosol characterization, *Remote Sens. Environ.*, *66*(1), 1–16.

Höpfner, M., and C. Emde (2005), Comparison of single and multiple scattering approaches for the simulation of limb-emission observations in the mid-IR, *J. Quant. Spectrosc. Radiat. Transfer*, *91*(3), 275–285.

Hsu, N. C., S. C. Tsay, M. D. King, and J. R. Herman (2004), Aerosol properties over bright-reflecting source regions, *IEEE Trans. Geosci. Rem. Sens.*, *42*(3), 557–569.

Jones, C., N. Mahowald, and C. Luo (2004), Observational evidence of African desert dust intensification of easterly waves, *Geophys. Res. Lett.*, *31*, L17208, doi:10.1029/2004GL020107.

Kerker, M. (1969), *The Scattering of Light, and Other Electromagnetic Radiation: Physical Chemistry*, *Monogr. Ser.*, vol. 666, Academic Press, New York.

Klüser, L., P. Kleiber, T. Holzer-Popp, and V. H. Grassian (2012), Desert dust observation from space—Application of measured mineral component infrared extinction spectra, *Atmos. Env.*, *54*, 419–427.

Kulawik, S. S., G. Osterman, D. B. Jones, and K. W. Bowman (2006), Calculation of altitude-dependent Tikhonov constraints for TES nadir retrievals, *IEEE Trans. Geosci. Rem. Sens.*, *44*, 1334–1342.

Laurent, B., B. Marticorena, G. Bergametti, P. Chazette, F. Maignan, and C. Schmechtig (2005), Simulation of the mineral dust emission frequencies from desert areas of China and Mongolia using an aerodynamic roughness length map derived from the POLDER/ADEOS 1 surface products, *J. Geophys. Res.*, *110*, D18S04, doi:10.1029/2004JD005013.

Laurent, B., B. Marticorena, G. Bergametti, and F. Mei (2006), Modeling mineral dust emissions from Chinese and Mongolian deserts, *Global Planet. Change*, *52*(1), 121–141.

Legrand, M., A. Plana-Fattori, and C. N'doumé (2001), Satellite detection of dust using the IR imagery of Meteosat: 1. Infrared difference dust index, *J. Geophys. Res.*, *106*(D16), 18,251–18,274, doi:10.1029/2000JD900749.

Legrand, M., O. Dubovik, T. Lapyonok, and Y. Derimian (2014), Accounting for particle non-sphericity in modeling of mineral dust radiative properties in the thermal infrared, *J. Quant. Spectrosc. Radiat. Transfer*, *149*, 219–240.

Mahowald, N. M., et al. (2001), Observed 20th century desert dust variability: Impact on climate and biogeochemistry, *Atmos. Chem. Phys.*, *10*(22), 10,875–10,893.

Mahowald, N., A. Baker, G. Bergametti, N. Brooks, R. Duce, T. Jickells, N. Kubilay, J. Prospero, and I. Tegen (2005), Atmospheric global dust cycle and iron inputs to the ocean, *Global Biogeochem. Cycles*, *19*, GB4025, doi:10.1029/2004GB002402.

Mahowald, N., J.-A. Ballentine, J. Feddema, and N. Ramankutty (2007), Global trends in visibility: Implications for dust sources, *Atmos. Chem. Phys.*, *7*, 3309–3337.

Marticorena, B., and G. Bergametti (1995), Modeling the atmospheric dust cycle: 1. Design of a soil-derived dust emission scheme, *J. Geophys. Res.*, *100*(D8), 16,415–16,430, doi:10.1029/95JD00690.

Menut, L., et al. (2013), CHIMERE 2013: A model for regional atmospheric composition modelling, *Geosci. Model Dev.*, *6*, 981–1028, doi:10.5194/gmd-6-981-2013.

Metzig, G. (1984), OPTIMA—Computation of the optical properties of single homogeneous or coated Mie-particles, *Kernforschungszentrum Karlsruhe GmbH, Lab. fuer Aerosolphysik und Filtertechnik*, 77.

Molina, M. J., and L. T. Molina (2004), Megacities and atmospheric pollution, *J. Air Waste Manag. Assoc.*, *54*(6), 644–680.

Moulin, C., H. R. Gordon, V. F. Banzon, and R. H. Evans (2001), Assessment of Saharan dust absorption in the visible from SeaWiFS imagery, *J. Geophys. Res.*, *106*(D16), 18,239–18,249, doi:10.1029/2000JD900812.

O'Neill, N. T., T. F. Eck, A. Smirnov, B. N. Holben, and S. Thulasiraman (2003), Spectral discrimination of coarse and fine mode optical depth, *J. Geophys. Res.*, *108*(D17), 4559, doi:10.1029/2002JD002975.

Peyridieu, S., et al. (2013), Characterisation of dust aerosols in the infrared from IASI and comparison with PARASOL, MODIS, MISR, CALIOP, and AERONET observations, *Atmos. Chem. Phys.*, *13*(12), 6065–6082.

Pierangelo, C., A. Chédin, S. Heilliette, N. Jacquinet-Husson, and R. Armante (2004), Dust altitude and infrared optical depth from AIRS, *Atmos. Chem. Phys.*, *4*(7), 1813–1822.

Pierangelo, C., M. Mishchenko, Y. Balkanski, and A. Chédin (2005), Retrieving the effective radius of Saharan dust coarse mode from AIRS, *Geophys. Res. Lett.*, *32*, L20813, doi:10.1029/2005GL023425.

Prospero, J. M. (1999), Assessing the impact of advected African dust on air quality and health in the eastern United States, *Human Ecol. Risk Assess.*, *5*(3), 471–479.

Prospero, J. M., P. Ginoux, O. Torres, S. E. Nicholson, and T. E. Gill (2002), Environmental characterization of global sources of atmospheric soil dust identified with the NIMBUS 7 Total Ozone Mapping Spectrometer (TOMS) absorbing aerosol product, *Rev. Geophys.*, *40*(1), 1002, doi:10.1029/2000RG000095.

Remer, L. A., et al. (2005), The MODIS aerosol algorithm, products, and validation, *J. Atmos. Sci.*, *62*(4), 947–973.

Rodgers, C. D. (2000), *Inverse Methods for Atmospheric Sounding: Theory and Practice*, World Scientific Comp., London.

Sayer, A. M., N. C. Hsu, C. Bettenhausen, and M.-J. Jeong (2013), Validation and uncertainty estimates for MODIS Collection 6 Deep Blue aerosol data, *J. Geophys. Res. Atmos.*, *118*, 7864–7872.

Schepanski, K., I. Tegen, B. Laurent, B. Heinold, and A. Macke (2007), A new Saharan dust source activation frequency map derived from MSG-SEVIRI IR-channels, *Geophys. Res. Lett.*, *34*, L18803, doi:10.1029/2007GL030168.

Schepanski, K., I. Tegen, and A. Macke (2012), Comparison of satellite based observations of Saharan dust source areas, *Remote Sens. Environ.*, *123*, 90–97.

Schmechtig, C., B. Marticorena, B. Chatenet, G. Bergametti, J.-L. Rajot, and A. Coman (2011), Simulation of the mineral dust content over Western Africa from the event to the annual scale with the CHIMERE-DUST model, *Atmos. Chem. Phys.*, *11*(14), 7185–7207.

Steck, T. (2002), Methods for determining regularization for atmospheric retrieval problems, *Appl. Optic.*, *41*, 1788–1797, doi:10.1364/AO.41.001788.

Stiller, G. P., et al. (2000), *The Karlsruhe Optimized and Precise Radiative Transfer Algorithm (KOPRA), vol. FZKA 6487 of Wissenschaftliche Berichte*, Forschungszentrum Karlsruhe, Germany.

Stiller, G. P., T. von Clarmann, B. Funke, N. Glatthor, F. Hase, M. Höpfner, and A. Linden (2002), Sensitivity of trace gas abundances retrievals from infrared limb emission spectra to simplifying approximations in radiative transfer modelling, *J. Quant. Spectrosc. Radiat. Transfer*, *72*, 249–280.

Su, X., P. Goloub, I. Chiapello, H. Chen, F. Ducos and Z. Li (2010), Aerosol variability over East Asia as seen by POLDER space-borne sensors, *J. Geophys. Res.*, *115*, D24215, doi:10.1029/2010JD014286.

Sugimoto, N., Y. Hara, A. Shimizu, T. Nishizawa, I. Matsui, and M. Nishikawa (2013), Analysis of dust events in 2008 and 2009 using the lidar network, surface observations and the CFORS model, *Asia Pac. J. Atmos. Sci.*, *49*(1), 27–39, doi:10.1007/s13143-013-0004-3.

Sun, J., M. Zhang, and T. Liu (2001), Spatial and temporal characteristics of dust storms in China and its surrounding regions, 1960–1999: Relations to source area and climate, *J. Geophys. Res.*, *106*(D10), 10,325–10,333, doi:10.1029/2000JD900665.

Tikhonov, A. (1963), On the solution of incorrectly stated problems and a method of regularization, *Dokl. Acad. Nauk SSSR*, *151*, 501–504.

Torres, O., A. Tanskanen, B. Veihelmann, C. Ahn, R. Braak, P. K. Bhartia, P. Veefkind and P. Levelt (2007), Aerosols and surface UV products from Ozone Monitoring Instrument observations: An overview. *J. Geophys. Res.*, *112*, D24S47, doi:10.1029/2007JD008809.

Vandenbussche, S., S. Kochenova, A. C. Vandaele, N. Kumps, and M. De Mazière (2013), Retrieval of desert dust aerosol vertical profiles from IASI measurements in the TIR atmospheric window, *Atmos. Meas. Tech.*, *6*, 2577–2591, doi:10.5194/amt-6-2577-2013.

von Clarmann, T., et al. (2003), Retrieval of temperature and tangent altitude pointing from limb emission spectra recorded from space by the Michelson Interferometer for Passive Atmospheric Sounding (MIPAS), *J. Geophys. Res.*, *108*(D23), 4736, doi:10.1029/2003JD003602.

Wang, K., Y. Zhang, A. Nenes, and C. Fountoukis (2012), Implementation of dust emission and chemistry into the Community Multiscale Air Quality modeling system and initial application to an Asian dust storm episode, *Atmos. Chem. Phys.*, *12*, 10,209–10,237, doi:10.5194/acp-12-10209-2012.

Winker, D. M., W. H. Hunt and M. J. McGill (2007), Initial performance assessment of CALIOP, *Geophys. Res. Lett.*, *34*, L19803, doi:10.1029/2007GL030135.

Winker, D. M., M. A. Vaughan, A. Omar, Y. Hu, K. A. Powell, Z. Liu, W. H. Hunt, and S. A. Young (2009), Overview of the CALIPSO mission and CALIOP data processing algorithms, *J. Atmos. Oceanic Technol.*, *26*(11), 2310–2323.

Worden, H. M., et al. (2007), Comparisons of Tropospheric Emission Spectrometer (TES) ozone profiles to ozonesondes: Methods and initial results, *J. Geophys. Res.*, *112*, D03309, doi:10.1029/2006JD007258.

Xu, X., J. Gao, J. Gao, and Y. Chen (1994), Air pollution and daily mortality in residential areas of Beijing, China, *Arch. Environ. Health*, *49*(4), 216–222.

Yang, P., Q. Feng, G. Hong, G. W. Kattawar, W. J. Wiscombe, M. I. Mishchenko, O. Dubovik, I. Laszlo, and I. N. Sokolik (2007), Modeling of the scattering and radiative properties of nonspherical dust-like aerosols, *Aerosol Sci.*, *38*, 995–1014.

Yoshioka, M., N. Mahowald, A. Conley, W. Collins, D. Fillmore, C. Zender, and D. Coleman (2007), Impact of desert dust radiative forcing on Sahel precipitation: Relative importance of dust compared to sea surface temperature variations, vegetation changes and greenhouse gas warming, *J. Clim.*, *20*, 1445–1467, doi:10.1175/JCLI4056.1.

Young, S., D. Winker, M. Vaughan, Y. Hu, and R. Kuehn (2008), Extinction retrieval algorithms, CALIOP algorithm theoretical basis document PC-SCI-202 Part 4. [Available at http://www-calipso.larc.nasa.gov/resources/pdfs/PC-SCI-202Part4v1.0.pdf.]

Yu, H., M. Chin, D. M. Winker, A. H. Omar, Z. Liu, C. Kittaka, and T. Diehl (2010), Global view of aerosol vertical distributions from CALIPSO lidar measurements and GOCART simulations: Regional and seasonal variations, *J. Geophys. Res.*, *115*, D00H30, doi:10.1029/2009JD013364.

Zhang, Q., B. Laurent, F. Velay-Lasry, R. Ngo, C. Derognat, B. Marticorena, and A. Albergel (2012), An air quality forecasting system in Beijing—Application to the study of dust storm events in China in May 2008, *J. Environ. Sci.*, *24*(1), 102–111.

Zhou, D. K., A. M. Larar, X. Liu, W. L. Smith, L. L. Strow, P. Yang, P. Schlussel, and X. Calbet (2011), Global land surface emissivity retrieved from satellite ultraspectral IR measurements, *Geosci. Rem. Sens. IEEE Trans.*, *49*(4), 1277–1290.